

Emission-line stars discovered in the UKST $H\alpha$ survey of the Large Magellanic Cloud; Part 1: Hot stars

Warren A. Reid^{1,2*} and Quentin A. Parker^{1,2,3*†}

¹*Department of Physics, Macquarie University, Sydney, NSW 2109, Australia*

²*Macquarie University Research Centre in Astronomy, Astrophysics & Astrophotonics, Macquarie University, Sydney, NSW 2109, Australia*

³*Australian Astronomical Observatory, PO Box 296, Epping, NSW 1710 Australia*

Accepted 2012 June 7. Received 2012 June 5; in original form 2012 February 1

ABSTRACT

We present new, accurate positions, spectral classifications, radial and rotational velocities, $H\alpha$ fluxes, equivalent widths and B,V,I,R magnitudes for 579 hot emission-line stars (classes B0 - F9) in the Large Magellanic Cloud (LMC) which include 469 new discoveries. Candidate emission line stars were discovered using a deep, high resolution $H\alpha$ map of the central 25 deg² of the LMC obtained by median stacking a dozen 2 hour $H\alpha$ exposures taken with the UK Schmidt Telescope (UKST). Spectroscopic follow-up observations on the Anglo-Australian Telescope (AAT), the UKST, the Very Large Telescope (VLT), the South African Astronomical Observatory (SAAO) 1.9m and the 2.3m telescope at Siding Spring Observatory have established the identity of these faint sources down to magnitude $R_{\text{equiv}} \sim 23$ for $H\alpha$ (4.5×10^{-17} ergs cm⁻² s⁻¹ Å⁻¹).

Confirmed emission-line stars have been assigned an underlying spectral classification through cross-correlation against 131 absorption line template spectra covering the range O1 to F8. We confirm 111 previously identified emission line stars and 64 previously known variable stars with spectral types hotter than F8. The majority of hot stars identified (518 stars or 89%) are class B. Of all the hot emission-line stars in classes B-F, 130 or 22% are type B[e], characterised by the presence of forbidden emission lines such as [S II], [N II] and [O II]. We report on the physical location of these stars with reference to possible contamination from ambient H II emission. Only 13 of the emission-line stars require additional high resolution spectroscopic observations in order to assign a spectroscopic classification. They have nonetheless been added to the catalogue.

Along with flux calibration of the $H\alpha$ emission we provide the first $H\alpha$ luminosity function for selected sub-samples after correction for any possible nebula or ambient contamination. We find a moderate correlation between the intensity of $H\alpha$ emission and the V magnitude of the central star based on SuperCOSMOS magnitudes and the Optical Gravitational Lensing Experiment (OGLE-II) photometry where possible. Cool stars from classes G-S, with and without strong $H\alpha$ emission, will be the focus of part 2 in this series.

Key words: stars: emission-line, Be - stars: rotation - Magellanic Clouds - surveys - stars: kinematics and dynamics - line: profiles.

1 INTRODUCTION

The Large Magellanic Cloud (LMC) is a unique laboratory in which to study the peculiar characteristics of massive and luminous emission-line stars. At a known distance of ~ 50 kpc (see Reid & Parker 2010 and references therein) to all

LMC members, modest inclination angle to the line of sight (~ 21 deg) and with relatively low interstellar extinction ($R_V = 3.41 \pm 0.06$; Gordon et al. 2003), apparent brightness is a good indicator of absolute luminosity to within a few tenths of a magnitude.

We take advantage of these benefits as we identify and begin basic analysis of emission-line stars in the LMC. The most prominent observational feature of the emission-line stellar group is the presence of the $H\alpha$ line. The presence of

* E-mail: warren.reid@mq.edu.au; war@aa0.gov.au (WR);

† E-mail: quentin.parker@mq.edu.au (QAP)

this emission feature has been widely used as an identifier in the many previous searches for emission-line stars in the LMC (eg. Feast et al. 1960; Henize 1956; Lindsay 1963, 1974; Bohannan & Epps 1974; Grebel 1997; Keller et al. 1999; Grebel & Chu 2000; Keller et al. 2000; Olsen et al. 2001). None of these surveys went particularly deep. More recently, the OGLE II database has prevailed as the main tool used to uncover emission-line star candidates (Sabogal et al. 2005).

The UKST $H\alpha$ survey of the central 25deg^2 of the LMC has changed this situation. It was adjunct to the successful Southern Galactic Plane $H\alpha$ survey (Parker et al. 2005) and has revealed large numbers of various emission objects. In addition to revealing 460 new planetary nebulae within the survey region which were confirmed spectroscopically (Reid & Parker, 2006a,b), spectroscopic followup and careful analysis has revealed 579 hot emission-line stars with spectral classes B-F out of a total sample of 1,062 emission-line stars of all spectral types uncovered. Only 111 of these were previously known or identified while 469 are newly discovered. The majority are Be, B[e], Bpe and HAeBe stars but two are Luminous Blue Variable (LBV) candidates. Identifying these objects will assist our understanding of the main sequence evolution of massive stars. We have also identified 6 new and 33 previously known Wolf-Rayet stars, which are not included in this number but will be the special focus of a follow-up paper.

Be stars are known to be variables which undergo active and quiescent stages (Telting 2000; Bjorkman et al. 2002). A single epoch survey could miss many of these stars if they were undergoing a quiescent stage. This problem has already been demonstrated by several follow-up investigations (Hummel et al. 1999; Keller et al. 1999; Wisniewski and Bjorkman 2006) which were unable to identify all of the previously identified Be stars in the Magellanic Clouds and in the Galaxy. In addition, these same follow-up studies revealed previously unidentified Be stars. Our $H\alpha$ survey, utilising 12 $H\alpha$ exposures taken over a three year period has largely alleviated such problems and revealed a large number of emission-line stars in the survey region to a magnitude of $R_{\text{equiv}} \sim 22$ for $H\alpha$.

In order to study the Balmer emission we have measured the Equivalent Width (EW) and Full Width Half Maximum (FWHM) of the $H\alpha$ emission-lines. In addition, we include $H\alpha$ fluxes from medium resolution spectroscopy of 575 (99.3%) of the detected emission-line stars within the survey area. Our follow-up spectroscopy was conducted from November 2004 to February 2005 on a variety of telescopes, allowing us to re-observe several known variable stars and detect minor changes in spectral characteristics. All but 2 candidate emission-line stars found in the $H\alpha$ survey had some degree of $H\alpha$ emission detectable in their spectrum at the time of observation. After describing flux calibration (section 5), we explain the method used to assign a spectral classification and luminosity class to each star using cross-correlation against well-established templates (section 6). Section 7 describes our method for deriving the rotational velocities and section 8 outlines a simple method for correcting or at least estimating nebula contribution in the spectrum. Section 9 details our routine for assigning accurate positions to each star.

In section 10 we describe the method used for measuring the radial velocity of each star. Velocities accurate to ~ 4 km

s^{-1} have been found for 572 emission-line stars using both the weighted emission-line and cross-correlation techniques on our higher dispersion spectroscopic data. These velocities can be used to search for kinematical substructures in the LMC disk, create a 3D kinematic map of the LMC for comparison with the HI disk, assist studies of age-metallicity dispersion and distribution, potentially find stellar associations and streams, and compare medium to old age populations such as planetary nebulae within the LMC (Reid & Parker 2006b).

In section 11 we show the projected distribution of emission-line stars and late-type stars across the survey field of the LMC. In section 12 we measure the intensity of the $H\alpha$ emission considering ambient sky and any nebula contamination in order to create the first luminosity function for these stars in the LMC. Then, in section 13 we assess the emission by comparing BVI photometry from SuperCOSMOS and OGLE-II data where available. We discuss the stellar photometry, its reliability and problems associated with variability. In section 14 we briefly discuss the variability already found in many of the candidate emission-line stars. The full catalogue of emission-line stars is described in section 15 and presented in the appendix. Individual spectra and $H\alpha$ images will be available (2nd half 2012) on a dedicated web page hosted by the Astronomy Department at Macquarie University.

2 BACKGROUND TO HOT EMISSION-LINE STARS

The origin of emission-lines in hot stars such as Be stars is not well understood. Such emission-line stars are found near the main sequence of luminosity classes V to III exhibiting Balmer emission (Jaschek et al. 1981, Frew & Parker 2010). Various mechanisms have been proposed to explain how gaseous circumstellar disks may form around Be stars (see Porter & Rivinius, 2003 for a review). Struve (1931) was the first to speculate that Be stars exhibit rapid rotation. Recent theoretical studies suggest that classical Be stars may be rotating close to their critical velocity (Townsend et al. 2004) and exhibiting a strange form of variability (Kaler 1997). Other models of circumstellar disk formation include the wind-compressed model (Bjorkman & Cassinelli 1993), pulsations arising from the stellar photosphere (Rivinius et al. 2001) and the magnetically torqued and wind compressed disk model (Cassinelli et al. 2002). While variables such as Cepheids and Miras are known to pulsate radially, many stars also pulsate non-radially, producing subtle magnitude variations and changing the shape of absorption lines. It has been suggested that these oscillations, common on the O and B main sequence, may be powerful enough to drive the winds which produce the Be phenomenon (Kaler 1997).

In the case of pre main sequence (PMS) T Tauri stars, the origin of the emission lines is understood in terms of the magnetospheric accretion model, where the emission lines originate from magnetospheric accretion columns (Uchida & Shibata 1985; Königl 1991; Hartmann et al. 1994; Muzerolle et al. 1998, 2001). With the detection of magnetic fields in a few Herbig AeBe stars (Hubrig et al. 2004; Wade et al. 2005), the magnetospheric accretion model was successfully

applied to these objects (Muzerolle et al. 2004). However, the mechanism for triggering the accretion is still not known.

B[e] stars have all the characteristics of Be stars but they additionally include forbidden emission lines in their spectra. Although lines such as [O III] λ 5007 are suggestive of planetary nebulae (PNe), the presence of Fe emission and He absorption in the strong blue continuum clearly separate B[e] stars from PNe.

The evolutionary sequence of these stars is still not well known. Nor is the non-spherically symmetric circumstellar environment which is responsible for the B[e] phenomenon. Strong variability often reported from these objects has been explained by outbursts and shell phases (Hutsemekers 1985; Andrillat & Houziaux 1991).

Related stars such as Herbig Ae/Be (HAeBe) stars, first discussed by Herbig (1960) are found above the main sequence on the HR diagram and are believed to be making their way toward it along radiative tracks as first postulated by Henyey et al (1955). Along with T Tauri stars, they share the characteristic of being associated with a nebula and infra-red emission indicating the presence of circumstellar dust (Hillenbrand et al. 1992; Lada & Adams, 1992). What immediately separates them from T Tauri stars is their larger mass of between $2M_{\odot}$ and $10M_{\odot}$. In order to separate HAeBe stars from B[e] supergiants, Waters and Waelkens (1998) included the condition that HAeBe stars should be of luminosity classes V to III.

As well as the Balmer lines, other optical emission-lines often observed in HAeBe emission-line stars include He I (λ 5876Å and λ 6678Å), O I (λ 7774Å and λ 8446Å) and the Ca II triplet (λ 8498Å, λ 8542Å and λ 8662Å) (Herbig 1960; Hamann 1994; Böhm & Catala 1994; Böhm & Hirth 1997; Corcoran & Ray 1998; Viera et al. 2003; Acke et al. 2005). We do not attempt to separate HAeBe stars from B[e] stars since many HAeBe and B[e] stars are spectroscopically indistinguishable.

3 OPTICAL OBSERVATIONS

3.1 The H α survey

Over a period of three years, from 1997, a series of repeated narrow-band H α and matching broad-band short red (SR) exposures of the central LMC field were taken in order to produce a deep H α and SR image with a 1 magnitude depth gain over a single image frame. The twelve highest quality and well-matched UK Schmidt Telescope 2-hour H α exposures and six 15-minute equivalent SR-band exposures were selected. From these exposures, deep, homogeneous, narrow-band H α and matching broad-band SR maps of the entire central 25 deg² region of the LMC were constructed.

The full aperture H α filter used for this survey was effectively the world's largest monolithic interference filter to be used in astronomy (Parker & Bland-Hawthorn 1998). The choice of central wavelength (λ 6590Å) and bandpass (70 Å FWHM) work effectively in the UKST's fast f/2.48 converging beam meaning the H α line remains within the filter band-pass for velocities up to 400 km s⁻¹. Peak filter transmission is >85%. The fields for the survey were exposed on non-standard, overlapping 4-degree centres due to the circular aperture of the H α filter. These overlapped fields enabled

full contiguous coverage of the entire LMC/SMC region in H α despite the circular aperture.

The successful implementation of high resolution, panchromatic Tech-Pan film on the UKST, coupled with its peak sensitivity at H α , was a prime motivation for the survey. Tech-pan film was an ideal wide-field photographic detector for use with an H α filter. The resulting images produced were unequalled in terms of their combined resolution, sensitivity and LMC coverage. Further details of the properties of Tech-Pan can be found in Parker & Malin (1999).

The SuperCOSMOS plate-measuring machine at the Royal Observatory Edinburgh (Hambly et al. 2001) was used to scan, co-add and pixel match these selected exposures creating 10 μ m (0.67 arcsec) pixel data which extends 1.35 (H α) and 1 (SR) magnitude deeper than individual exposures, achieving the full canonical Poissonian depth gain, e.g. Bland-Hawthorn, Shoppell & Malin (1993). This gives a depth \sim 21.5 for the SR images and $R_{\text{equiv}} \sim$ 22 for H α (4.5×10^{-17} ergs cm⁻² s⁻¹ Å⁻¹) which is at least 1 magnitude deeper than the best wide-field narrow-band LMC images previously available. An accurate world co-ordinate system was applied to yield sub-arcsec astrometry (see section 9), essential for success of the spectroscopic follow-up observations.

3.2 Emission-line star discovery technique and criteria

The deep UKST H α survey of the LMC was originally undertaken in order to uncover multiple compact emission sources. Our successful search for extremely faint PNe (Reid & Parker 2006a,b) is proof of its worth. It soon became clear, however, that the depth and resolution of the maps allowed us to also search for low luminosity stellar sources which exhibit detectable emission-lines. Since our aim was to uncover faint sources, we largely ignored extremely bright stars, whether or not they exhibited H α emission. Many of the better known, bright emission-line stars in the LMC will therefore not appear in this work. What we have included in our survey is a large sample of emission-line star candidates that comply with the expected luminosity of brightest LMC PNe (M_B 13 - 24).

Candidate emission-line stars were found using an adaptation of a technique available within KARMA, first reported in Reid & Parker (2005). The SR images were assigned a false red colour and merged with the H α narrow-band images assigned a blue colour. Careful selection of software parameters allowed the intensity of the matched H α and SR .fits images to be perfectly balanced allowing only peculiarities of one or other pass-band to be observed and measured. Using this technique, normal continuum stars appear uniformly pinkish in colour. Emission objects such as H II regions and PNe are strongly coloured blue. The broader point spread function (PSF) of the H α line in emission-line stars creates a faint blue aura around the star, allowing them to be easily detected. Figures 1 to 5 show a small 30 \times 30 arcsec area of the stacked SR and H α maps featuring Be stars, RPs255, RPs256, RPs285, RPs286 and RPs338¹ respectively

¹ RPs refers to Reid Parker star

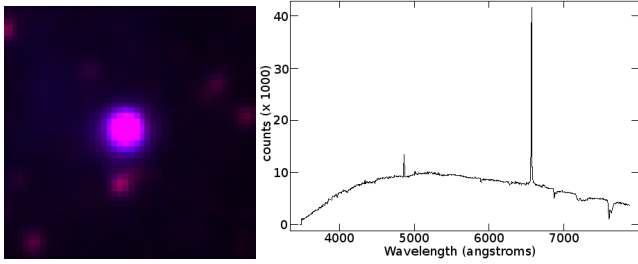


Figure 1. $H\alpha/R$ 30×30 arcsec image and 2dF low resolution spectrum of RPs255 also known as BE474 (Bohannon & Epps, 1974) and as L333 (Lindsay, 1963). $M_{H\alpha}=16.37$. Compact $H\alpha$ emission 9.6 arcsec dia is largely due to PSF. North is upwards.

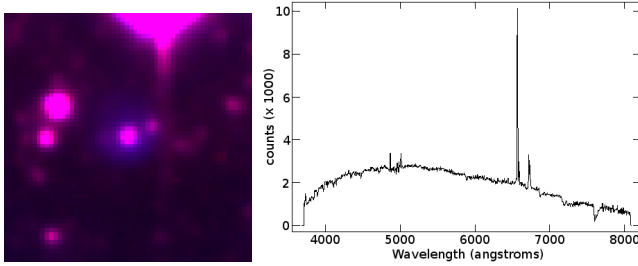


Figure 2. Same as above for newly discovered emission-line star RPs256. $M_{H\alpha}=19.34$. Forbidden lines lead to B[e] classification.

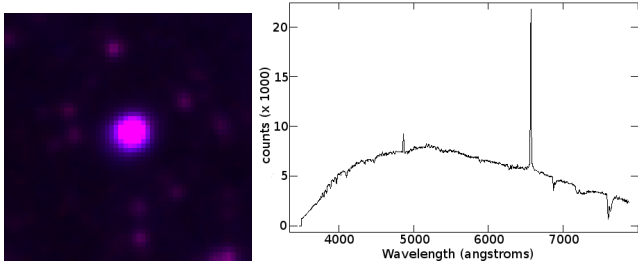


Figure 3. Same as above for RPs285 also known as BE411 (Bohannon & Epps, 1974). $M_{H\alpha}=16.92$.

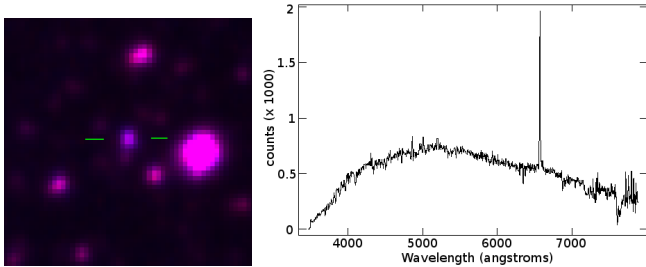


Figure 4. Same as above for RPs286 also known as BE426 (Bohannon & Epps, 1974). $M_{H\alpha}=19.37$. Only 2.4 arcsec dia on the image including minor PSF contribution.

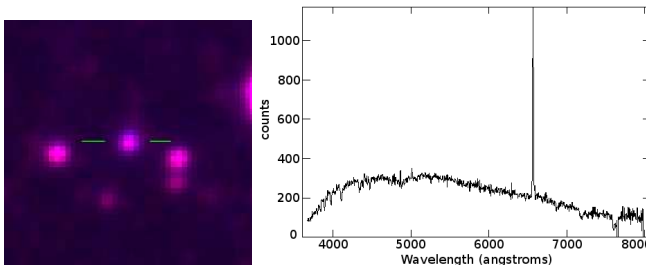


Figure 5. Same as above for newly discovered emission-line star RPs338. $M_{H\alpha}=20.19$. Only 2.8 arcsec dia. on image.

at the centre together with their confirmatory 2dF spectrum. Spectroscopic confirmation shows us that the wider and more diffuse halo seen surrounding examples such as RPs256 (Figure 2) strongly indicates the presence of forbidden lines in the spectrum, leading to its classification as a B[e] star.

Even with a narrow band $H\alpha$ filter, the presence of faint Balmer lines in LMC emission-line stars can be very difficult to detect. Although it can be quite easy to miss such faint sources, the colouring and merging of the maps makes detection straightforward, preventing objects above a certain EW threshold from being overlooked and allowing the full depth gain of the maps to be utilized.

4 SPECTROSCOPIC CONFIRMATION OF CANDIDATE EMISSION-LINE STARS

Having used the stacked $H\alpha$ and SR maps to catalogue over 2,000 emission sources, a large follow-up spectroscopic programme was undertaken in order to identify and classify each source. The most effective and efficient way to follow-up such a large number of objects was to use wide-field multi-object spectroscopic (MOS) systems such as 2dF on the Anglo-Australian Telescope (AAT), 6dF on the UK Schmidt Telescope (UKST) and FLAMES on the Very Large Telescope (VLT). Bright, extended emission objects were selected to be observed individually using long-slit spectroscopic systems on the South African Astronomical Observatory (SAAO) 1.9m telescope and the Mount Stromlo and Siding Spring Observatory (MSSSO) 2.3m telescope.

In Table 1 we summarise details regarding the spectroscopic follow-up observations. The field names are observation identifications or object names in the case of the 2.3m observations. Each of these multi-fibre observations have different central coordinates. The first three 2dF fields, with prefix ST..., are service time runs. Classical observations using 2dF on the AAT provided 15 pointings of 1 degree radius labeled A to O. FLAMES observations on the VLT provided 9 field pointings with an 11 arcminute radius. The FLAMES observations were centred on several of the densest areas on the LMC main bar. The three fields observed with 6dF on the UKST were repeated, subsequently with a different set of stars and extended objects, maximising use of the wide 6 arcsec fibres.

4.1 2dF observations

A five night observing run on the AAT using 2dF (Lewis et al. 2002) was undertaken in December 2004 to spectroscopically confirm LMC emission candidates. The identification of peculiarities associated with $H\alpha$ excess in various object types (see Reid & Parker 2006a for more details) indicated that we could expect our candidates to be a mixture of PNe, compact H II regions, and emission-line stars such as Be, Ae, WRs, T Tauri, M giants, carbon stars and a number of symbiotics. 2dF was an ideal choice of instrument for the spectroscopic follow-up of large numbers of candidate emission objects due to its unique ability to simultaneously observe 400 targets (including objects, fiducial stars and sky positions) with 2 arcsec fibres over a wide 2 degree diameter

Table 1. Observing logs for LMC Emission-line object follow-up. In some instances the same object has been observed multiple times at different resolutions and in overlapping fields.

Field Name	Telesc.	Date	Grating Dispenser	Dispersion Å/pixel	Central λ (Å)	Coverage λ (Å)	T _{exp} s	N _{exp}	N _{obj}
2dF-ST1	AAT	26 Nov-03	300B	4.299	5841	3650 - 7960	1500	2	131
2dF-ST2	AAT	26 Nov-03	300B	4.299	5841	3650 - 7960	1500	2	80
2dF-ST3	AAT	15 March-03	300B	4.299	5852	3660 - 7970	1800	2	81
a1550,061-213	1.9m	09-13 Nov-04	300	5	5800	3850 - 7738	800	2	11
a1550,214-324	1.9m	11-15 Nov-04	1200	1	6563	6000 - 7120	1000	2	10
FLAMES 1-9	VLT	5-7 Dec-04	LR2	0.339	4272	3960 - 4567	1000	3	420
FLAMES 1-9	VLT	5-7 Dec-04	LR3	0.339	4797	4500 - 5077	1000	3	420
FLAMES 1-9	VLT	5-7 Dec-04	LR6	0.339	6822	6438 - 7172	1000	3	420
2dF A-O	AAT	13-16 Dec-04	300B	4.3	5852	3660 - 7970	1200	3	3603
2dF-1200R A-O	AAT	17-18 Dec-04	1200R	1.105	6793	6220 - 7340	1200	2	3303
RP's	2.3m	07-18 Jan-05	600R+B	2.2	4600	3600 - 5570	900	2	56
RP's	2.3m	07-18 Jan-05	600R+B	2.2	6563	5515 - 7520	900	2	56
6dF 1-3	UKST	3-5 Feb-05	425R	0.62	6750	5318 - 7576	600	3	573
6dF 1-3	UKST	3-5 Feb-05	580V	0.62	4750	3948 - 5600	600	3	573

field area. The large corrector lens incorporates an atmospheric dispersion compensator, which is essential for wide wavelength coverage using small diameter fibres.

The observations provided $\sim 4,000$ spectra. Individual exposure times were mostly 1200s using the 300B grating with a central wavelength of 5852\AA and wavelength range $3600\text{-}8000\text{\AA}$ at a dispersion of $4.30\text{\AA}/\text{pixel}$. These low-resolution observations, at 9.0\AA FWHM, were the primary means of object identification and were used in cross-correlation to provide spectral classifications. All fields were then re-observed using the higher resolution 1200R grating to gain our radial velocities with wavelength range $6220\text{-}7340\text{\AA}$.

4.2 ESO VLT FLAMES observations

Our data includes additional spectroscopic observations in dense regions of the LMC main bar, undertaken using the multi-object fibre spectroscopic system, FLAMES (Pasquini 2002) on the VLT UT2 over three nights in December 2004. The OzPoz positioner on FLAMES was used to position the 130 available fibres with an accuracy of better than 0.1 arcsec. Gratings LR2 and LR3 allowed us to cover the most important optical diagnostic lines for emission-line stars in the blue including [O III] $\lambda 4363$, He II $\lambda 4686$, H β and [O III] $\lambda 4959$ & $\lambda 5007$ in emission and absorption lines such as He I $\lambda 4471$, $\lambda 4387$, $\lambda 4144$, $\lambda 4121$, $\lambda 4026$, $\lambda 4009$ and $\lambda 3820$. Grating LR6 covered the H α , [N II] $\lambda 6548$ and $\lambda 6583$ lines as well as the [S II] $\lambda 6716$ & $\lambda 6731$ lines. Using these low resolution gratings allowed us to both identify and classify objects and observe micro-structures such as self-absorption within the Balmer emission lines. The observed FLAMES 25 arcmin diameter fields, containing a total of 420 objects, overlapped with 2dF fields, providing a continuous coverage of the main bar region.

4.3 6dF observations

A 3 night observing run was also undertaken on the 3-5th February 2005 using the 6dF 150 fibre MOS system on the

UKST. Each of these observations covered an impressive 6 degree diameter field on the sky and allowed us to observe candidates that were missed in 2dF observations due to crowding. The separate 580V and 425R gratings provided continuous coverage across the optical range from 3700\AA to 7550\AA for 573 objects observed. A proportion close to 50% were re-observations of objects previously covered using 2dF, providing additional object confirmation. The wider 6 arcsec fibres on 6dF, compared to the 2 arcsec fibres on 2dF, meant that we had to re-examine the location of each object in order to avoid observing close stellar sources with that instrument. On the other hand, the 6 arcsec fibre meant that it was an excellent choice of instrument for extended sources such as large PNe with post AGB halos and compact H II regions.

4.4 Long-slit observations

Long-slit spectra were obtained using the 1.9m telescope at the South African Astronomical Observatory in November 2004 and 2.3m telescope at Mount Stromlo and Siding Spring Observatory (MSSSO) in January 2005. Both of these observing runs not only provided spectra for object confirmation and classification but assisted our flux calibration for fibre-based observations. Individually, the 1.9m telescope provided both low dispersion spectra for object identification and higher resolution spectra for radial velocities. Light fed to the double-beam spectrograph on the MSSSO 2.3m telescope was split by a dichroic and sent to red and blue optimised detectors. The resulting medium resolution red and blue spectra also provided spectroscopic confirmation of individual objects that were missed during multispec-observations due to overcrowding on field plates.

4.5 Reduction of spectra

The 2dF data were reduced using the sophisticated 2dFDR reduction software provided by the Australian Astronomical Observatory (AAO) specifically for the reduction of 2dF

multi-fibre spectra. The software performed the standard reduction procedures of bias and dark subtraction, flat fielding, sky subtraction, tram-line mapping to the fibre locations on the CCD, fibre extraction, arc line identification, wavelength calibration and fibre throughput calibration as well as providing a user interface with several options, specific to 2dF multi-fibre reductions. Specific bias frames are not required as the software simply makes use of the under-scan/overscan bias strips on each CCD exposure.

The FIT method of fibre extraction was used as it simultaneously fits Gaussians to the spectrum being extracted and to the two either side of it, allowing the amount of overlap at each point along the spectrum to be evaluated. This method also minimises contamination between fibres and was applied to all the reductions.

To perform the sky subtraction, the data was first corrected for the relative fibre throughput, based on a throughput map derived from about 15 dedicated sky fibres which were carefully selected across the 2dF field to avoid stars and ambient emission. The relative intensities of the skylines in the object data frame were used to determine the relative fibre throughput. This method saves time, as no off-set sky observations were required.

Cosmic rays were rejected either automatically during the process of combining two or more observations on the same field setup. This method was used because under certain circumstances the spatial profile is sometimes sensitive to the spectral structure of the data and it can mistake a strong emission-line for a cosmic ray.

Raw data from 6dF on the UKST was reduced using a tailored 6dF variant of the same (2dFDR) data reduction software. A specific input file informs the software that 6dF data is to be reduced. Like 2dF, a separate file relating to the specific grating must be used. Again, cosmic rays were rejected automatically during the process of combining two or more observations of the same field.

VLT FLAMES data were reduced using the pipeline system provided by ESO through the ‘GASGANO’ Java-based data file organiser developed and maintained by ESO. This graphic interface identifies the input file types, produces a master bias, flat, and dark frame, then reduces and combines the science frames.

The 2.3m and 1.9m telescope spectra were reduced using the standard long-slit IRAF tasks IMRED, SPECRED and CCDRED and FIGARO’s task BCLEAN. Cosmic rays were rejected when combining frames. One-dimensional spectra were created and the background sky was subtracted. Final flux calibration used the standard stars LTT7987, LTT9239, LTT2415 and LTT9491.

5 FLUX CALIBRATION OF THE 2DF FIBRE SPECTRA

The large proportion of objects observed with 2dF means that a reliable flux calibration of the LMC stellar emission-lines was required in order to compare stellar spectra from different 2dF fields, to make meaningful comparisons between fibre spectroscopy and long-slit observations of individual objects, and to create a luminosity function.

Altogether, 18 overlapping 2dF fields, 9 FLAMES fields and 6 6dF multi-object fields were observed in order to cover

the entire central 25deg² survey region of the LMC. To calibrate the resulting data counts, we used PNe with low continuum levels and well determined fluxes gained from HST observations (see Reid & Parker 2006a, 2006b). These objects were deliberately included and observed on each field plate for use as flux calibrators for each individual field.

The process involved matching each spectral line on each field plate from each CCD camera to raw PN fluxes gained from HST exposures. The individual H β and H α 2dF line intensities for known PNe observed on each CCD and each field plate exposure were plotted against HST-gained published fluxes for the same lines (see Figure 2 in Reid & Parker, 2010).

The agreement of flux-calibrated PNe from each spectrograph/field plate combination was considered robust enough (within 0.2 dex) to allow calibration to all the H β and H α emission-lines for other emission objects observed in the same field. In each case, a line of best fit was derived and the underlying linear equation extracted. This equation became the calibrator for each emission-line in each object where the CCD and individual 2dF field plate exposure was the same. Full details including a discussion on the reliability of the method are presented in Reid & Parker (2010).

6 SPECTRAL CLASSIFICATION

Spectral classification of all the emission-line stars was undertaken to assist in various studies such as the distribution of emission by stellar population, the estimation of central star temperatures, creation of H-R diagrams and improving our understanding of Balmer emission in stars of varying temperatures. We touch on some of these issues later in this paper.

6.1 Method of classification

To assign a spectral classification, it is necessary to measure the strengths and widths of various absorption features which depict specific stellar temperatures and surface gravities, independent of any associated emission characteristics. To assist this process we used standard stellar spectra supplemented by 10 LMC emission-line stars from our sample with recognised spectral classifications as templates. The spectral standards were based on observations available from Jacoby et al (1984), Turnshek et al (1985), Silva and Cornell (1992), Pickles (1998) and Le Borgne et al. (2003).

The classification of emission-line stars is complex and often problematic due to their variability and atmospheric activity. The strength and profile of the Balmer lines in emission only lend moderate assistance to classification, although the equivalent width of H γ can be a good indicator of spectral type and luminosity in main sequence stars (Underhill & Doazan 1982). In the spectra of young stars such as T Tauri stars, photospheric absorption lines can be filled in or disguised by UV radiation from accretion hotspots (Hartigan et al. 1995; Gullbring et al. 1998), making classification difficult. Further complication arises from active Post Main Sequence (PMS) stars where most spectral lines are in emission (Cohen & Kuhl, 1979; Hernández et al., 2004). These

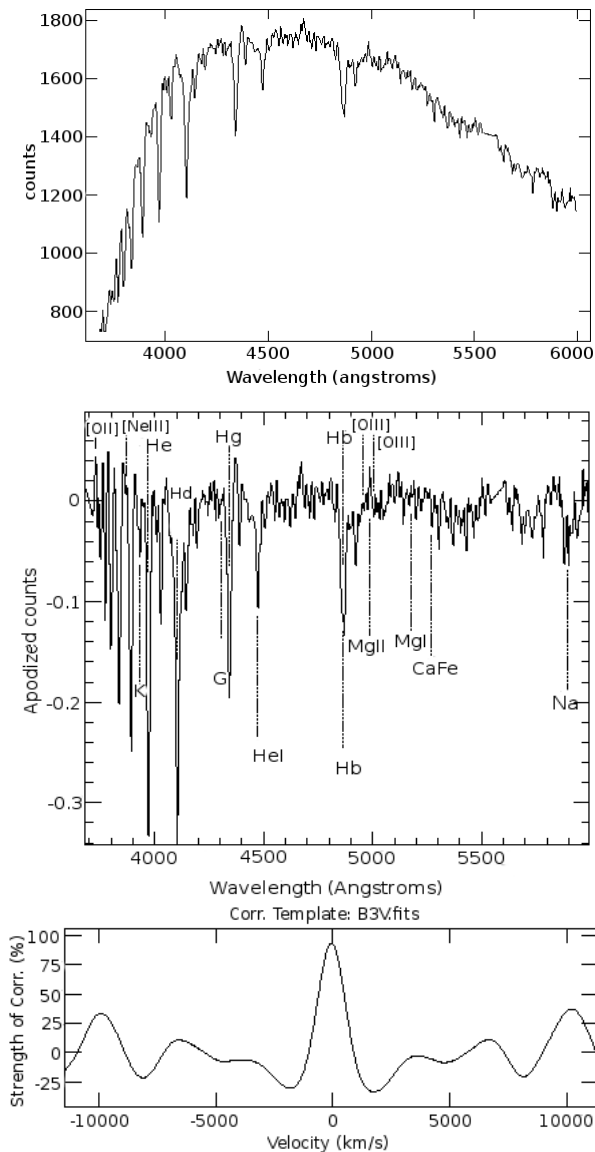


Figure 6. The top image shows the blue end of the RPs1326 optical spectrum prior to the removal of emission-lines and continuum. The centre frame shows the apodized and continuum subtracted spectrum, created within XCSAO and used in cross-correlation to match the best fitting template. The lower frame shows the strength of the resulting correlation, represented by the central gaussian curve, once the task has found the best-fitting template.

types are usually denoted as ‘continuum stars’ since it is virtually impossible to accurately assign a spectral type.

Due to the large number of emission-line stars to be classified in this survey, as a first step, a cross-correlation routine was employed. Although the IRAF XCSAO task was originally developed in order to cross correlate galactic spectra against templates and gain redshifts (Tonry and Davis, 1979), it works equally as well as a spectral classification tool with stellar templates. The task identifies the closest spectrum in terms of line strengths and widths found and then returns a velocity along with the name of the best matching

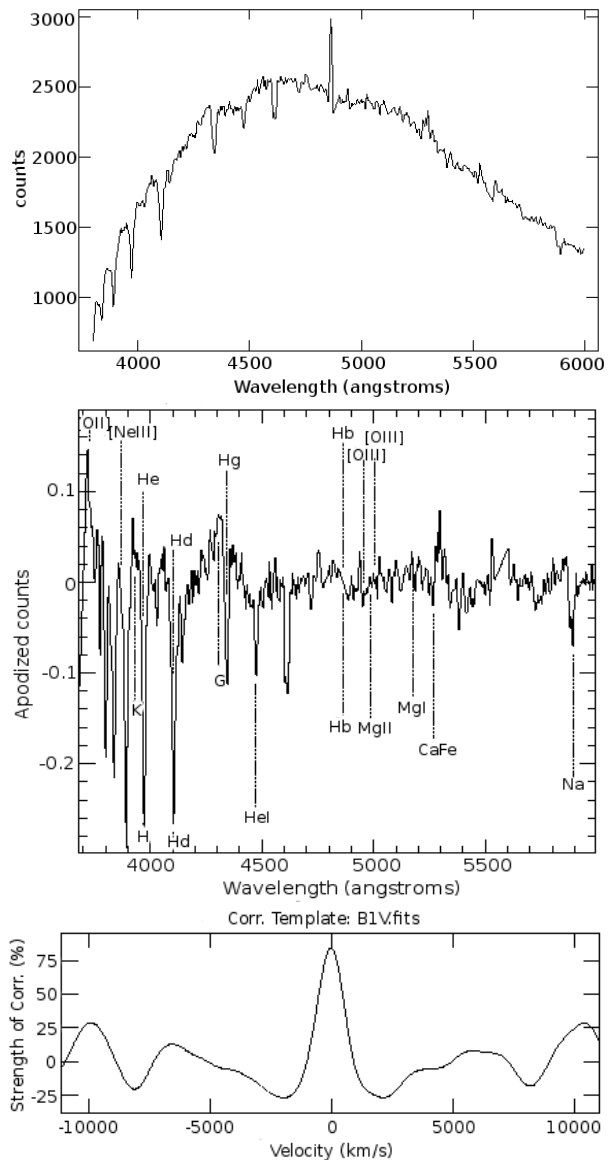


Figure 7. The same as Figure 6 but showing the blue end of the RPs1262, a B1V optical spectrum with top: the original blue end including emission-lines and continuum prior to their removal, middle: the continuum-subtracted and apodised spectrum with detected lines identified automatically by the software, bottom: the correlation.

template through cross-correlation based on fourier transformations.

In order to produce the most accurate result, emission-lines (mainly the Balmer series and any residual telluric sky lines which can effect the cross-correlation) were removed. The continuum was then removed using the IRAF CONTINUUM task in order to cross-correlate the absorption lines alone. This negated the influence of the continuum where it was either stronger or weaker than the best matching spectrum in the templates, which were also continuum subtracted. Apodization within XCSAO uses a cosine bell to attenuate data on the ends of the spectrum, reducing high wave number fourier components that would be produced by abrupt cutoffs at the ends of the spectra, effectively smooth-

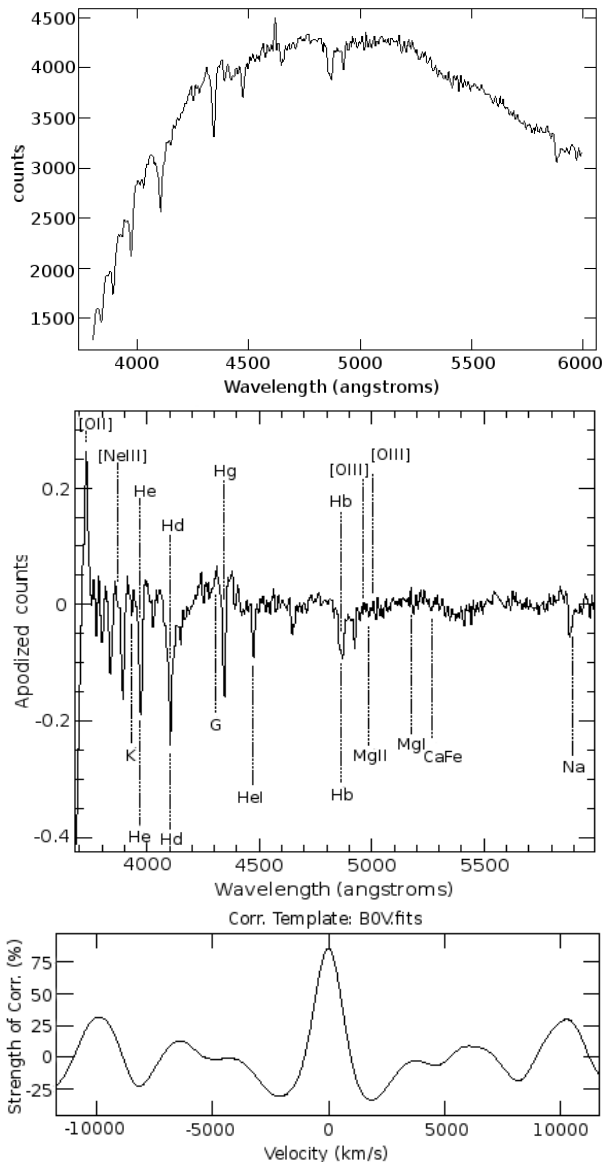


Figure 8. The same as Figure 6 but showing the blue end of RPs1367, a B0V optical spectrum with top: the original blue end including emission-lines and continuum prior to their removal, middle: the continuum-subtracted and apodized spectrum, bottom: the correlation.

ing out the continuum across the full length of the spectrum. Examples are shown in figures 6, 7 and 8 using only the blue end of the optical spectrum which contains the main diagnostic lines for spectral classification. The same is not true for late-type G to SC stars. For these stars, removal of emission-lines is still necessary but the overall shape of the spectrum becomes increasingly important with decreasing spectral type. By late K types it was already necessary to match the continuum with the templates using the wider optical spectrum ($\lambda 3700$ to $\lambda 8000$).

Having run the above-mentioned tasks, the raw spectra, including the emission lines, were then inspected and measured. B-type stars are strongly characterised by He and Balmer emission-lines. He I lines show a very broad intensity maximum by B2 and B3. The intensity of Balmer lines

remains almost constant for Supergiant stars from B0 Ia through to A0 Ia but strengthens in late B giants. For main sequence stars, however, the Balmer lines strengthen from B0V to A0V. A more precise spectral type can therefore be confirmed by defining the ionisation temperature of Si and He supplemented by C II and C III. The main luminosity criteria are summarised in Table 2. In early B and late A main sequence through to F stars, line ratios are much easier to use for identification due to the larger number of lines available. The luminosity class can be tested by assessing the wings of the Balmer lines, which widen from classes I to V.

By applying these criteria, we re-classified 40 Be stars which were automatically classified as luminosity class I supergiants in the cross-correlation routine. Most of these were re-identified as giants or subgiants. Fast rotation of the Be stars causes the Balmer lines to broaden thereby matching spectra to supergiant stellar templates. This effect was countered by examining each spectrum with reference to the ratios as shown in Table 2.

6.2 Results of spectral classification

Although this paper is presenting the hot emission-line stars, it is important to note that the UKST $H\alpha$ survey also uncovered a large number of cooler G to SC stars which either emit strongly or are bright at $H\alpha$. These late stellar objects, which will be the subject of a second paper of this series, are listed briefly here in order to compare detection rates.

The majority of emission stars found have been classified as Be, [Be] (V - III) stars and M (III) giant stars. The letter ‘e’ indicates that, at the very least, the first member of the Balmer series ($H\alpha$) is in emission. Although we identified 13 supergiant B stars with $H\alpha$ emission, these types are not generally known as Be stars, a classification reserved for luminosity classes V, IV and III. Table 3 provides a quick breakdown of the various emission-line stars found in the central 25deg^2 LMC survey. Of these stars, 64 Be stars are previously known variable stars.

Figure 9 shows the spectral classification of the identified B to K emission-line stars in our survey. The number of stars found is subdivided by luminosity class according to the Morgan-Keenan system (Morgan et al. 1943) where the width of absorption lines are a measure of the size of the star and thus the total luminosity. As per the standard convention, class I are supergiants, class III are giants and class V are main sequence stars. It is clear that the largest number of emission-line stars found belong to class B and, of those, the supergiants are mainly found at B0. These supermassive stars again dominate our detections from classes G5 to K5. The largest spectral class of Be stars represented in our sample are those on the main sequence.

6.3 Types of emission-line stars found

Of the 468 newly discovered emission-line stars, we identified 107 B[e] stars that exhibit forbidden emission-lines. They were found in spectral types B0-B9. The most common forbidden emission-lines found in the B[e] stars were [Fe II] $\lambda 4244, 4287, 4415, 5273, 7155$, [O I] $\lambda 6300, 6363$, [N I] $\lambda 5755, 6548, 6584$, [S I] $\lambda 4068, 6717, 6730$, [O II] $\lambda 7320, 7330$, and [O III] $\lambda 4959, 5007$, the most frequent being

Table 2. The most important lines examined to assist in follow-up spectral classification after cross-correlation. These include the ratios and equivalent widths of the Balmer lines and the ratios of classification lines in the $\lambda 3500$ - 4800 region of B-type stars. It should be noted that the ratios shown in columns 2-5 more or less depend on the luminosity. For example, He I is only weakly visible in A0 supergiants.

Class	Ratios & EW	Ratios	Ratios (later types)	Ratios (latest types)
Supergiants				
B0 Ia-B2 Ia	$H\alpha/H\beta/H\gamma$	He II 4542/He I 4471 He II 4200/He I 4144	Si III 4552/Si IV 4089	C III 4068/[O II] 4076 C II 4267/He I 4121
B2 Ia-B5 Ia	$H\alpha/H\beta/H\gamma$	Si III 4552/Si IV 4089	C III 4068/[O II] 4076	C II 4267/He I 4121
B5 Ia-A0 Ia	$H\alpha/H\beta$	Si II 4128,31/He I 4121	Si II 4128,31/He I 4026	Si II 3856, 63/He I 3820, 4026
Giants				
O5 III-B0 III	$H\alpha/H\beta/H\gamma$	He II 4200, 4542/He I 4471	Si IV 4089/H δ	He I 4388/H γ
B0 III-B5 III	$H\alpha/H\beta/H\gamma$	Si IV 4089/Si III 4553	C III 4647-51/He I 4388	Mg II 4481/He I 4471
B5 III-A0 III	$H\alpha/H\beta$	Mg III 4481/He I 4471	Si II 4128,31/He I 4144,4026	
Main Sequence				
O4 V-B0 V	$H\alpha/H\beta/H\gamma$	He II 4542/He I 4471	He II 4686/He I 4922	Si IV 4089/He I 4144
B0 V-B5 V	$H\alpha/H\beta/H\gamma$	Si IV 4089,4116/He I 4121	He II 4686/He I 4713	C III 4068-70/He I 4009 C III 4647-51/He I 4713
B5 V - A0 V	$H\alpha/H\beta$	Si II 4128,31/He I 4144,4026	Mg II 4481/He I 4471*	C II 4267/Mg II 4481

* The He I $\lambda 4471$ line is all but gone in main sequence stars by B8 V.

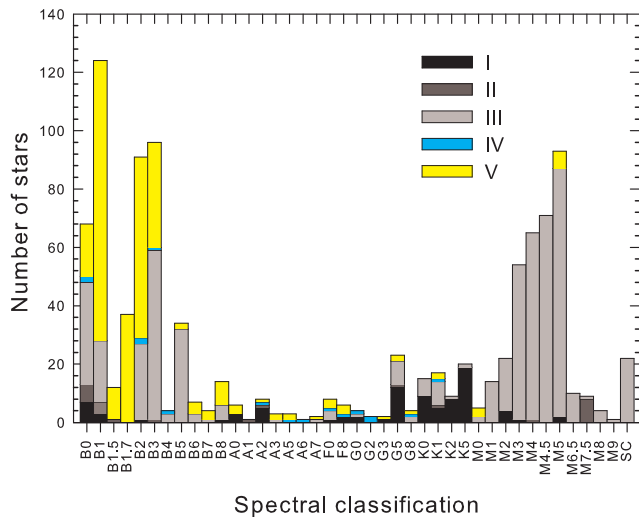


Figure 9. Distribution of all types of emission-line stars found within our survey region of the LMC according to number and spectral classification. The number of stars in each class is subdivided in order to express the luminosity class of the star according to the Morgan-Keenan system. It is clear that there are more main sequence stars, bright in $H\alpha$ emission, within the B spectral class. Class SC may be divided into $4 \times SC4/9$ stars, $1 \times S4/2$, $1 \times S4/6$ and 16 carbon stars, 13 of which are C6.

[Fe II] and [O I]. The ionisation potentials of the last two, less than 25eV, place them lower than the ion energies found in planetary nebulae.

We have also identified early B-type stars with anomalies (weak or strong) in carbon, nitrogen and usually oxygen. These were first labelled CNO stars by Jaschek & Jaschek (1967). The stars with anomalies in their heavier elements are called Bp stars, where ‘p’ designates ‘peculiar’. We have identified 5 Bp candidates. They are particularly enhanced in Si- $\lambda 4200$, Mn II, Cr II, Eu II and Sr II.

As the cores of intermediate mass stars ($M_* = 1-8M_\odot$)

Table 3. Classification of stellar emission sources for the whole catalogue. The numbers provided in column 4 are not additional but represent the number of stars previously known as variable.

Object Type	Previously known	Newly discovered	known variable
O stars		1	
Be stars	82	306	55
B[e] stars	23	107	9
Ae stars	3	29	
F stars	3	25	
G stars		29	
K stars		49	
M stars	86	315	33
WR stars	33	6	
Carbon stars		16	
CVs	4		4
Eclipsing Binaries	3		3
LBVs		2	
Bp stars	2	5	
AGB stars	4		
Symbiotic stars		18	
hot stars without id.		14	
cool stars without id.		7	

become too depleted in hydrogen for fusion reactions, they leave the main sequence to ascend the Red Giant Branch (RGB) and Asymptotic Giant Branch (AGB). At this point, the stars are seen as Miras or OH/IR stars with maser activity (Winckel, 2003). Although these stars will become the central stars of planetary nebulae, they are not yet hot enough to ionise a potential vast halo of expelled material. Nevertheless, the dense, complex atmospheric matter, including possible extended circumstellar envelopes, is ionised sufficiently to be detected in $H\alpha$ and [N II].

The second largest group of stars uncovered in this survey are the M giants. Due to their cooler temperature, these stars have a spectral energy distribution (SED) that peaks towards the red end of the spectrum. They often exhibit strong excess $H\alpha$ emission originating from the chromo-

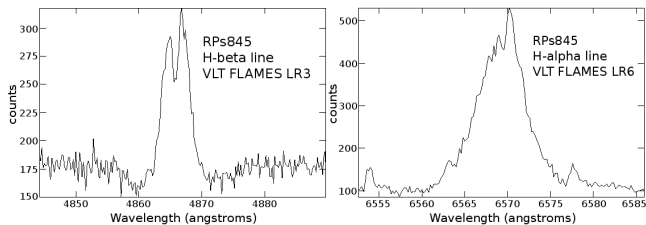


Figure 10. An example of Balmer line splitting where we can see fine structure components. These profiles often feature three or more emission peaks and minute detailed features extending down to the continuum. The example shown is RPs845 with H β left (FLAMES LR3 grating) and H α right (FLAMES LR6 grating). The absorption wings of the H β line are also greatly broadened by the Stark effect indicating that these are main sequence stars where the gravity and electron pressure is large.

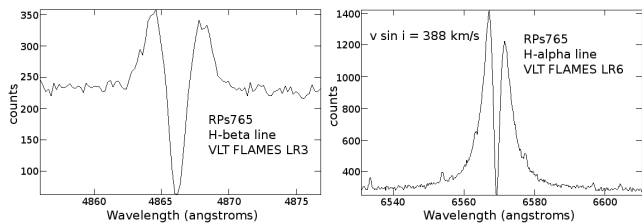


Figure 11. An example of Balmer line splitting, typical of a ‘shell star’ or more correctly, a star going through a shell phase, where the central absorption on the H α line extends below the stellar continuum. The example shown is RPs765 with H β left (FLAMES LR3 grating) and H α right (FLAMES LR6 grating).

sphere which strengthens with increasing spectral type or decreasing luminosity. For this reason the H α line cannot be used as a classification criteria and was removed prior to cross-correlation.

Late-type M giants feature TiO and VO bands which strengthen with decreasing temperature. They also feature Mg λ 5167,5173,5184 until M4III and M6.5V as well as NaI λ 5890,5896 although the latter can be overwhelmed by TiO absorption in stars later than M2III.

Our survey uncovered 401 M giant stars with emission, 315 of which are newly identified. Of the 86 previously known M giants, 33 have been found to have variable luminosity. These M giants, together with a number of G and K emission-line stars will be the subject of the next paper in this series.

6.4 Observed emission line profiles

The emission line profiles can represent a combination of instrumental broadening, small absorption features which are often broadened by rotation originating from the photosphere of the star, and the emission-line profile produced by the star’s circumstellar envelope. Both emission and absorption lines may include kinematic and non-kinematic broadening from effects such as radiative transfer and Thomson scattering which affect the envelope (eg. Hanuschik, 1989). Absorption lines are generally less affected by such effects leaving emission lines to provide important information about the rotation and physical conditions affecting the star and it’s circumstellar envelope.

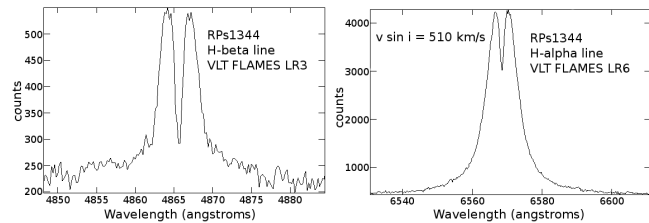


Figure 12. An example of Balmer line splitting in the high velocity circumstellar emission of RPs1344 with H β left (FLAMES LR3 grating) and H α right (FLAMES LR6 grating). The narrow profile of the shell absorption line indicates its origin closer to the outer, slowly rotating parts of the shell.

The Balmer emission lines demonstrate the most diverse range of profiles. Profile variations are believed to be dependent on the observer’s angle of inclination to the star’s pole. According to the model of Struve (1931), shell profiles occur where the star is viewed equatorially ($i = 90$ deg), double peaked profiles occur at mid-inclination angles and singly peaked profiles occur by viewing towards the pole ($i = 0$ deg). The measurement of accurate inclination angles, however, is complicated by other influences on the emission profile such as temperature, density and rotational velocity (Underhill & Doazan, 1982; Quirrenbach et al. 1997; Miroshnichenko et al. 2001).

We present some representative examples of Balmer emission profiles using our VLT observations. Several of the Be stars in our VLT-observed sample show some shallow double reversal more or less central to the H α line. Some stars also have emission profiles with three emission peaks. It is these fine structure components (see Figure 10) that are known to show the greatest variability, down to the order of hours (Hubert & Floquet, 1998). Stars whose emission lines have sharp, very deep absorption cores such as the example shown in Figure 11 have come to be known as *shell* stars. The intrinsic variability of Be stars, however, has proven that over time these stars can lose and regain these shell characteristics (Underhill & Doazan, 1982). We therefore refer to them as going through a ‘shell phase’ at the time of our observation. Following the convention proposed by Hanuschik et al. (1996), we formally identify a shell star where the central absorption extends below the stellar continuum.

Further to this definition, we add that this only applies to absorption on the H α line. The H β line is more dramatically affected by the atomic absorption since the reversal feature is not dependent or correlated to the strength of any individual Balmer emission line. For example, a medium absorption of H α resulting in a small reversal feature will correspondingly extend very deeply into the H β emissive flux (see Figure 12).

Asymmetry is a sub-feature found in a small percentage of Be star profiles. This is currently thought to arise from one-armed density waves in the circumstellar disk, also known as the global disk oscillation model (Silaj et al. 2010). In Figure 13 we show asymmetry where the reversal is left of centre while Figure 14 shows reversal to the right of centre, affecting both H β (left example) and H α (right example) Balmer lines the same way. The resulting emission peak on the left is known as the Violet (V) component and the emis-

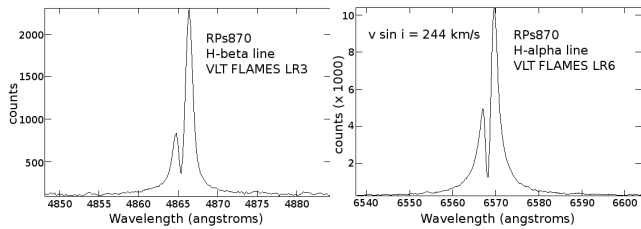


Figure 13. RPs870 is an example of Balmer line splitting which appears to the left of centre with H β left (FLAMES LR3 grating) and H α right (FLAMES LR6 grating). The peak R>V affects both hydrogen emission lines and arises from one-armed density waves in the circumstellar disk.

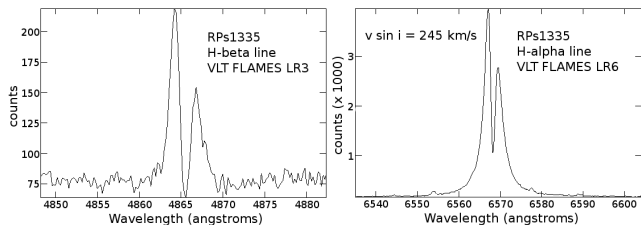


Figure 14. RPs1335 is an example of Balmer line splitting which appears to the right of centre with H β left (FLAMES LR3 grating) and H α right (FLAMES LR6 grating). In this case V>R.

sion peak on the right is known as the Red (R) component. These asymmetries are also seen in single emission-lines and are probably the result of minor or isolated density waves.

A more unusual feature among the Be star emission line profiles is the ‘wine-bottle’ shape, often produced by viewing the star near to the pole. The example shown in Figure 15 is possibly broadened by a combination of disk rotation and Thomson scattering.

In attempting to classify the profiles of H α emission according to the particular features mentioned above, it is prudent to refer only to the higher resolution VLT FLAMES data. Figures 16 and 17 provide a comparison of the VLT FLAMES LR6 and 2dF 1200R spectra for the one object. In the first comparison (Figure 16) the strong absorption feature seen in RPs1343 using LR6 on FLAMES is only de-

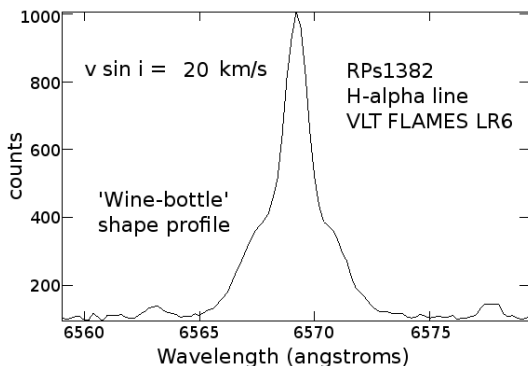


Figure 15. RPs1382 is an example of a ‘wine-bottle’ profile which may occur by viewing the rotating star close to pole-on ($i = 0$ deg angle). The low rotation velocity is a direct result this viewing angle and is measured using the central profile of the H α line (see section 7). The broadening is circumstellar.

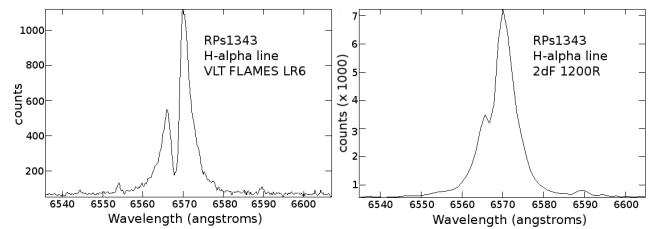


Figure 16. A comparison of H α Balmer line splitting in emission-line star RPs1343 as seen with the FLAMES LR6 R8600 grating (left) and the 2dF 1200R grating (to the right). The VLT spectrum with its increased detail provides the clear detection of line splitting and some microstructure. The 2dF spectrum is able to detect the presence of line splitting but the amplitude of the same is unable to be measured due to the lower resolution of the 1200R grating. No microstructure can be seen in the 1200R spectrum.

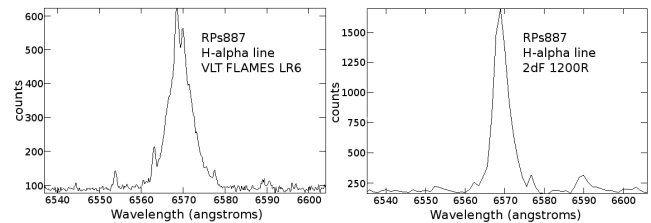


Figure 17. A comparison of H α Balmer line splitting in emission-line star RPs887 as seen with the FLAMES LR6 R8600 grating left and the 2dF 1200R grating to the right. The VLT spectrum shows fine line splitting to the top right but this cannot be seen in the 2dF 1200R spectrum which has a dispersion of 1.105Å/pixel. In this case the peaks at the top of the H α line are separated by 1.4Å, making fine detail impossible to detect at the lower resolution.

Table 4. H α profile features found in 122 emission-line stars observed with VLT FLAMES using the LR6 grating. Micro features are miniature peaks identified on the sides and at the top of a main peak.

Main feature	Total number	% of total	Number of micro features	Number of bottle shape
Single peak	100	82	11	9
Double peak V=R	10	8	2	
Double peak R>V	6	5	3	
Double peak V>R	4	3	3	
Shell	2	2	2	

tectable to a limited extent in the 2dF spectrum to the right. In the second comparison (Figure 17) the absorption feature is too narrow to be detected at a resolution of 1200R.

Using only the 122 emission-line stars observed on the VLT, the features shown in Table 4 were present. All 122 stars in this table reside within a 3 deg² region on the main optical bar of the LMC. With 100 detections, the single peak profile is the most common. At the time of spectroscopic observation, 11 stars were found to exhibit micro features such as miniature structures on the sides and/or at the peak. In time these may develop into separate peaks or disappear completely. Since emission-line stars are constantly evolving, a table such as this can only provide a snapshot of the percentage of features found at that time.

7 ROTATIONAL VELOCITIES

Classical Be stars undergo rapid rotation and possess geometrically thin, circular gaseous disks resulting in hydrogen Balmer emission (Jaschek et al. 1981; Porter & Rivinius 2003). Typical rotation compared to critical velocity (v_{eq}/v_{crit}) has been estimated at $\sim 70\%$ - 80% (Porter 1996; Porter & Rivinius 2003). A lower estimate of 40% - 60% of the critical breakup velocity for such stars was found by Cranmer (2005) but this set of data is not homogeneous. It is likely that both of these estimates may not take all the physical conditions into account. Due to fast rotation it is expected that the star is flattened, causing a variation in temperature and density from pole to equator. This is expected to result in a gravitational darkening of the stellar disk. Based on this theory, Townsend et al. (2004), employing the effects of equatorial gravity darkening, suggest that a degeneracy in the measurement of rotational rates allows Be stars to be rotating at or near their critical breakup velocity. An estimate of rotational velocity for the LMC set of emission-line stars will provide vital information for future studies.

Although the fine structure across the top of the Be star emission-line profile makes FWHM rather complex to untangle, the strength of the $H\alpha$ line negates any underlying photospheric biases or broadening. This is also true in cases where emission is weak. To derive the projected rotational velocity ($v \sin i$) we used the correlation found by Dachs et al. (1986, Equation (7)) with improvements made by Hanuschik (1989). Their three parameter correlation between FWHM ($H\alpha$), $v \sin i$ and equivalent width (EW) lead them to the relation:

$$\log[\text{FWHM}(H\alpha)/1.23 (v \sin i + 70\text{kms}^{-1})] = -0.08 \log EW + 0.14 \quad (1)$$

which was presented as equation (5) in Hanuschik (1989). We used this equation in the form:

$$v \sin i = [(\text{FWHM}(H\alpha) + 10^{0.08 \log EW + 0.14})/1.23] - 70 \quad (2)$$

to derive $v \sin i$ for all stars in our sample. The resulting relation between $\text{FWHM}(H\alpha)$ and $v \sin i$ is shown in Figure 18. The scatter is mainly due to the equivalent width of the individual line although there will inevitably be a contribution from non-kinematic line broadening due to radiation transfer (Poeckert and Marlborough, 1978), electron scattering, possible turbulence and measurement errors. The median fit to the data in Figure 18 yields

$$\text{FWHM}(H\alpha) = 0.89 v \sin i + 79\text{kms}^{-1}. \quad (3)$$

A histogram giving the frequency of $v \sin i$ for all hot emission-line stars in our LMC sample is shown in Figure 19. The distribution covers in excess of 500 km s^{-1} with a maxima at around 200 km s^{-1} . With the exception of 30 stars measured using 6dF, all the measurements were taken using the highest resolution 2dF, AAOmega and VLT data. The 30 stars measured using the 6dF red arm 0.62 \AA/pxel data cover a large range from $73 < v \sin i < 489$, indicating that the 6dF data is not introducing any bias to the overall results.

The number of stars found in the 50 km s^{-1} bin appears to be overstated in relation to the general trend seen in the histogram. This isolated rotational velocity peak probably has little to do with the spectral type or luminosity class,

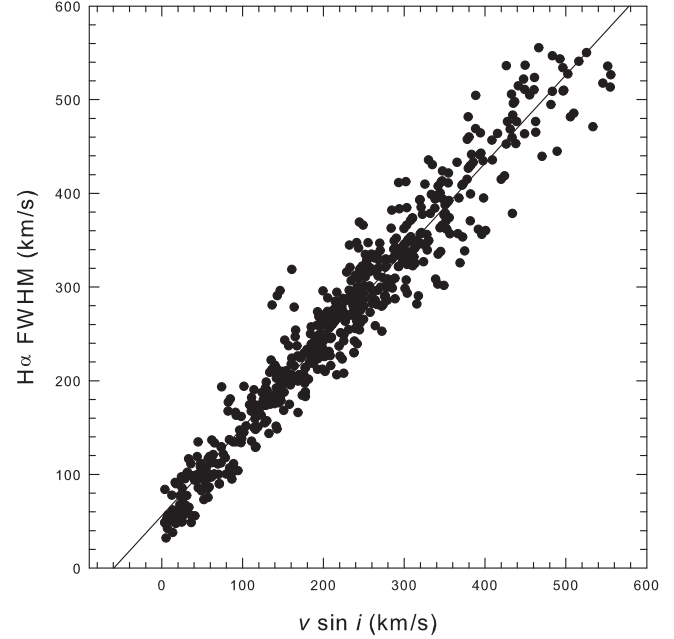


Figure 18. The relation between FWHM measured on the $H\alpha$ line and the rotational velocity ($v \sin i$) using equation (3) for all emission-line stars in our sample. The variations away from the line of equality are mainly due to the equivalent width, used to determine $v \sin i$.

both of which are quite evenly distributed across the histogram. It most likely reflects the number of stars we are viewing close to pole-on (see section 6.4), many of which do not display a strong wine-bottle $H\alpha$ emission profile. As with all surveys, the reason may also partly lie in our selection criteria, as we specifically targeted faint stars with relatively strong $H\alpha$ emission.

The process of estimating rotational velocities using FWHM and EW on $H\alpha$ emission lines which display a strong wine-bottle profile is somewhat complex. Measurement of these parameters using a line such as $\text{He}\lambda 4471$ is generally considered more accurate because it is less affected by circumstellar rotation. The extra-wide (wine-bottle profile) wings on these particular $H\alpha$ lines substantially increase both measurements, thereby giving these stars a typical rotational velocity between $200 < v \sin i < 300 \text{ km s}^{-1}$.

We have found that by measuring FWHM and EW on the $\text{He}\lambda 4471$ absorption line, or by fitting a gaussian curve to the $H\alpha$ wine-bottle profile, the rotational velocity readings drop substantially to levels below 100 km s^{-1} . Since both methods of measurement yield similar results ($5 < v \sin i < 40 \text{ km s}^{-1}$), we prefer to fit a Gaussian profile to the $H\alpha$ line. This is expected to produce the most accurate measurement of FWHM, EW and $v \sin i$ using these peculiar profiles. It not only constrains all FWHM and EW measurements to the $H\alpha$ line for direct comparison across the table (Appendix Table 1) but improves reliability due to the strength of $H\alpha$ compared to the $\text{He}\lambda 4471$ absorption line, which is weak, difficult to fit and often perturbed by the envelope.

After selecting LMC Be stars between classes B0 and

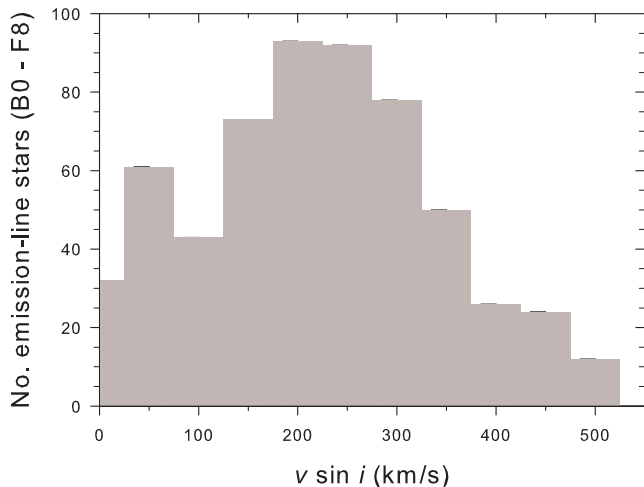


Figure 19. The distribution of estimated rotational velocities ($v \sin i$) for all the hot emission-line stars (B0 - F8) in our survey. The large number of stars occupying the bin at 50 km s^{-1} is most likely due to their near pole-on angle to our line of sight.

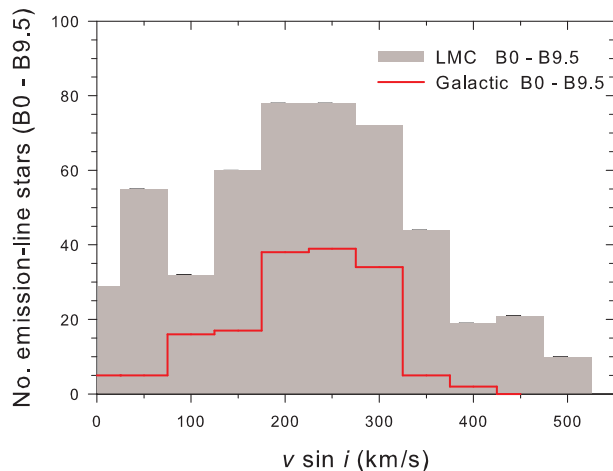


Figure 20. The distribution of rotational velocities ($v \sin i$) for all Be stars (B0 - B9.5) in our LMC sample compared to the distribution for Galactic Be stars (B0 - B9.5) found by Slettebak (1982).

B9.5, we have compared their distribution to the distribution found in the Galaxy for the same Be classes using data from Slettebak (1982). From the histogram in Figure 20 we find a correlation coefficient of 0.88 between the LMC and Galactic data sets. Although both data sets are not complete in any sense, the plot indicates that, based on a random selection, the majority of Be stars have a projected rotational velocity between $200 < v \sin i < 300 \text{ km s}^{-1}$.

8 NEBULA CONTRIBUTION

Approximately 15 percent of the emission-line stars in our sample are B[e] stars which show evidence of forbidden nebula emission lines such as [Fe II] $\lambda 4244, 4287, 4415, 5273, 7155$, [N II] $\lambda 6583, 6548$, [O I] $\lambda 6300, 6363$, [O II] $\lambda 7320, 7330$ and [S II] $\lambda 6716, 6731$ in their spectrum. Importantly, not all of these lines are necessarily to be found in every B[e] star but the most common are [Fe II] and [O I]. These stars are often associated with ambient or extended nebula emission which is ionised by the central star with surface temperatures of between 10,000 K and 33,000 K. This means that the H α line may be a combination of central star and nebula emission, making them difficult to separate when the RVs of each component are similar and/or when spectral resolution is not sufficient to distinguish the components.

Since the strength of the H α line in each star and the ambient background H α emission affecting the spectrum are constantly changing with location in the LMC, a general sky subtraction may be insufficient in some cases. Each object located in an area of diffuse H II emission must therefore be individually assessed for ambient nebula contribution on the basis of H α emission within a 10 arcsec radius of the star, which provides a fair estimate in the crowded regions of the LMC. This can be closely approximated using our deep H α map. The measurement of H α intensities on and off the emission-line star produces a ratio which roughly indicates the percentage of H α spectral flux emitting from the star. If the background emission is deemed to be contributing more than 10% of the measured flux, a special note about the B[e] status is made in the comments column of Appendix Table 1. If there is no ambient emission surrounding or in the immediate vicinity of the star, we may safely assume that the star is of the B[e] variety, where we expect to find emission-lines of [N II], [S II], [O II] and even [O III].

In Figure 21 we show an example of a B[e] star with a very significant contribution of emission lines normally associated with nebulae. Where emission lines are this strong we examine the immediate environment for ambient nebula emission. If the deep H α image shows us that much of the emission is environmental, we flag (in the comments column) that the other emission lines in the spectrum may be the result of ambient emission. In Figure 22 we show a regular B[e] star with some nebula lines present but no apparent environmental contribution requiring correction. Finally in Figure 23 we show a Be star requiring no nebula subtraction for environmental reasons and no nebula lines. All of these stars are located within a 1 degree radius of each other, emphasising the importance of surveying the immediate location of each star.

9 NEW ACCURATE POSITIONS FOR LMC EMISSION-LINE STARS

We found that emission-line star positions provided by many earlier surveys (mostly using the FK4 system) were not sufficiently accurate when converted to the J2000 equinox and compared to positions across our astronomically accurate survey. As many as 138 previously identified emission-line stars were only published with an accuracy to one decimal fraction of a minute. The majority of these also gave no

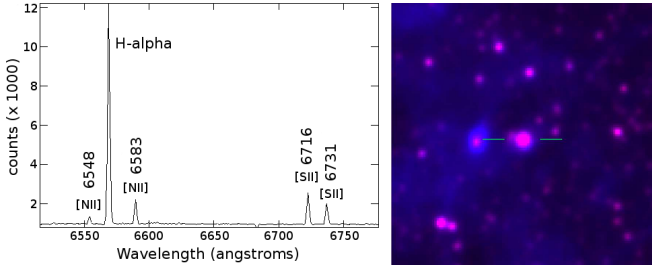


Figure 21. Left: A 2dF 1200R grating example of the red spectral region around the H α line in B[e] star RPs226 where there is strong emission from [N II] λ 6583,6548 and [S II] λ 6716,6731. Right: We show the H α (blue) and short red (red) combined UKST image, clearly showing the local environment and the contribution from ambient nebulous flux. Using the H α map alone we can estimate the proportion of nebula contribution by using the Starlink GAIA task to measure the ambient H α (sky) emission within 10 arcsec (\sim 2.4pc) of the star and compare the flux to that at the rim of the star, which represents the H α excess (H α -R) emission from the star. The object, 2 arcsec to the east of RPs226 (immediate left in the image) is RP225, a compact HII region.

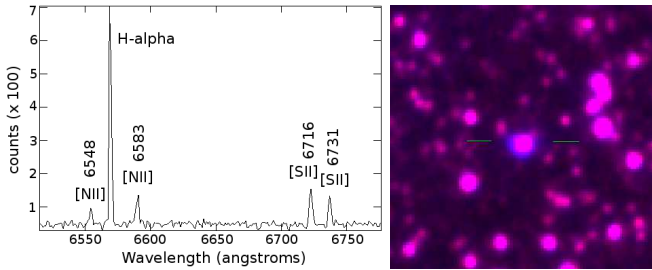


Figure 22. Left and right images as described in Figure 21 above. This is an example of a B[e] emission-line star (RPs161) with nebula lines present but no contribution from ambient emission at the stars location. No correction to the H α flux is required.

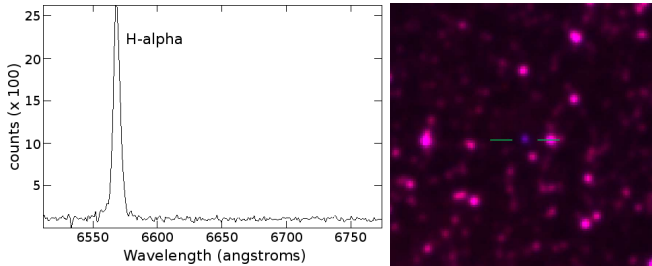


Figure 23. Left and right images as described in Figure 21 above. An example of a Be emission-line star (RPs634) not requiring any correction to the measured H α flux. No standard nebula forbidden emission-lines are detected and the environment is free of low level ambient emission.

seconds in DEC. Many true positions were uncertain given the crowded nature of the LMC. In many cases the known emission-line star had to be carefully verified as the object that was previously found. The K-view program in KARMA initially allowed us to find the position of peak intensity of any point source within the stacked H α /SR images allowing accurate positioning to 0.6 arcsec due to our meticulous calibration of our entire map with the SuperCOSMOS world coordinate system.

To improve the positioning and find the most accurate

positions for our new emission-line stars, we extracted red image data from the SuperCOSMOS Image Analysis Mode (IAM). The SuperCOSMOS plate measuring machine samples some 1,000 objects within 10 x 10 armin areas in order to define the xy-to-RA/Dec transformation. The resulting coordinates of a given pixel are thought to be accurate to a few tenths of an arcsec. Using both the H α /SR discovery images and accurate SuperCOSMOS image positions, we matched each emission-line star to the position provided by the IAM data. This match also allowed us to extract the SuperCOSMOS derived B and R broadband magnitudes for each star, as discussed in section 12.

10 RADIAL VELOCITIES

Stellar radial velocities for hot B stars are useful for kinematic studies within the LMC. They provide a valuable tool with which to compare young and old populations. Importantly, the radial velocities allow us to verify that our selected emission-line stars reside within the LMC.

Our stellar radial velocities were determined from the medium resolution 2dF 1200R, 6dF 425R and FLAMES spectra as described above. The largest number of velocities (92%) were measured using the 1200R 2dF grating which has an estimated accuracy of ± 4 km s $^{-1}$. Two different methods of velocity measurement were employed in order to reduce errors arising as a result of the application of a particular technique. These techniques have been described in Reid & Parker (2006b) and will only be repeated briefly here.

Initially, we used the IRAF EMSAO technique for measuring multiple, specified emission lines. Wavelengths for 13 common emission-lines within the λ 6200-7350 \AA range were specified to three decimal places. The program found the central position of each available line which was independent of the line width and self-absorption features. It then applied a weighted gaussian fit to each emission line dependent on its intensity, derived a weighted average across the spectrum and corrected for the heliocentric velocity. The EMSAO-derived velocity for each star was displayed and examined.

The second method of velocity determination involved the cross-correlation technique using XCSAO in IRAF (Kurtz & Mink, 1998). This method requires a list of template spectra with low internal velocities and accurately determined published radial velocities against which all the other spectra may be compared for measurement. Template emission-line velocities were based on a minimum of four lines, with at least two of these being fitted by EMSAO (Kurtz & Mink, 1998). Twenty LMC planetary nebula and emission-line star templates with well established velocities were chosen for the cross-correlation.

To derive a best possible radial velocity from our emission-line and cross-correlation methods, we examined the error and other properties (such as the fit and number of lines used) relating directly to each measurement system. From EMSAO, we used weighted velocity results where a large proportion of fitted lines were used in the compilation and error values ≤ 13 km s $^{-1}$. These error values sum and weight the difference in emission line velocities for a given object. Errors larger than this value begin to result from increasingly complex shell velocity structure. Error values up to 13

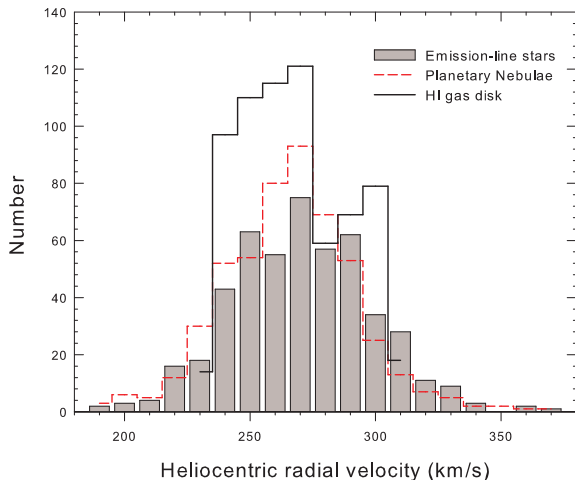


Figure 24. The distribution of LMC emission-line star velocities in our survey is shown by number and compared to the distribution for PNe and the HI gas disk. All sources have been placed into 10 km s^{-1} heliocentric radial velocity bins. The emission-line stars lie within the range found previously for LMC PNe and H II regions which is about 40 km s^{-1} wider at each end than the HI distribution. All three distributions share a mean peak number of sources at 270 km s^{-1} . The HI has a sudden trough after the peak (280 km s^{-1}) due to a warp which lies north of the main bar along the line of nodes (see Reid & Parker 2006b).

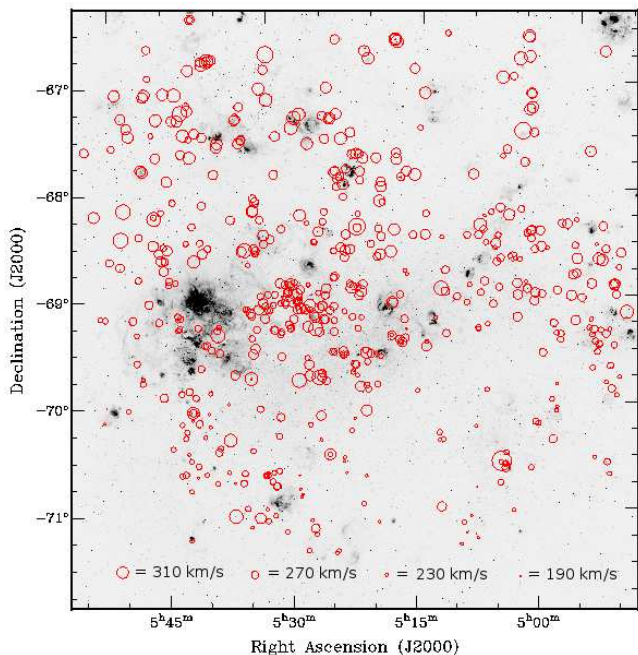


Figure 25. An $\text{H}\alpha$ map of the central 25deg^2 region of the LMC showing the distribution of hot emission-line stars as open red circles, the size of which indicates the measured heliocentric radial velocity. The larger the diameter, the higher the velocity. The circle sizes represent a linear scale but are magnified $10\times$ in order to emphasize similarities and contrast the deviations within selected areas. Similar to the HI gas disk, the PNe and H II populations, there is a noticeable gradient from high velocities NE of the main bar to low velocities SW of the main bar. The average velocity of 270 km s^{-1} for emission-line stars is also common to all three populations on the main bar.

km s^{-1} were to be expected using this technique, as velocity ratios between different lines (eg. $\text{H}\alpha$ and $[\text{N II}]\lambda 6583$) can vary depending on shock waves within the surrounding shell and/or in a few cases, ambient emission surrounding the star. In the cross-correlation technique, we looked for high correlation peaks and low error values $\leq 2\text{ km s}^{-1}$. In general, we favoured the cross-correlation technique since $>50\%$ of the target stars show only Balmer lines in emission and in many cases a weighted result was not possible with EMSAO. Results from EMSAO were used where errors from the cross-correlation were above 13 km s^{-1} .

A small percentage of these radial velocities will combine the true radial velocity with stellar atmospheric effects where the envelope is undergoing a phase of contraction or expansion. The contribution from these motions, unlikely to be much more than 50 km s^{-1} , will not unduly displace these stars away from their location in the LMC. The Balmer and shell lines used for our radial velocities are formed in the cooler outer atmosphere. The lower order $\text{H}\alpha$ line is formed in the outer layers of the atmosphere and is less affected by the large velocity variations which can affect the higher members of the Balmer series which are formed at the deepest layers of the envelope. According to the Struve's (1931) model, the mass flux of the star and its excitation steadily decreases towards a distance of several stellar radii where the emission lines are formed.

Our velocities, measured in the envelope, are lower than the escape velocity at the photosphere for stars with high $v \sin i$ found from photospheric He I lines, which are in turn broad, weak and often perturbed by the envelope. Since each emission-line star is individualistic in terms of its $v \sin i$, shell structure, phase, periodic and non-periodic radial motions and amplitudes, a weighted average and cross-correlation of the emission line in the outer atmosphere is the most efficient and accurate means of applying a radial velocity to each emission-line star in our catalogue.

In figure 24 we show a histogram of the heliocentrically corrected radial velocities for 501 of the hot emission-line stars in our survey. These are compared with our heliocentric velocities for 515 LMC PNe (Reid & Parker, 2006b) and 686 HI gas disk pointings from the LMC map of Rohlfs et al. (1984), covering the entire 25deg^2 survey region. Each pointing averages an $\sim 11.45\text{ arcmin}^2$ sub-region, ensuring an unbiased and fully representative distribution and mean can be obtained. The comparison shows that emission-line star velocities lie within the acceptable velocity boundaries and conform well with other LMC population types such as PNe and the HI gas (also see Reid & Parker, 2006b).

LMC emission-line stars and PNe have a very similar distribution but a wider range compared to the HI disk. Although 483 (89%) of the emission-line stars occupy the HI range 230 km s^{-1} to 310 km s^{-1} , the 52 outliers are to be expected since the HI disk has a narrow vertical velocity dispersion ranging between 17 km s^{-1} and 2.2 km s^{-1} with a mean of 6 km s^{-1} compared to PNe (45 km s^{-1} to 3 km s^{-1} ; mean 22 km s^{-1}) and emission-line stars (43 km s^{-1} to 3 km s^{-1} ; mean 23 km s^{-1}), found by sampling $37 \times 37\text{ arcmin}$ sub-regions across the survey area. A few large dispersions in HI can indicate a splitting of the gas disk, which occurs in regions such as the leading arm (see Reid & Parker 2006b). The central peak of 270 km s^{-1} is common to all three distributions and indicates a strong midpoint incorpo-

rating both young and old populations. The sudden trough at 280 km s^{-1} for the HI gas disk is further proof of a sharp warping of the disk which runs north of the main bar in a SE to NW direction, close to the line of nodes (see Reid & Parker 2006). This warping produces a large velocity dispersion and fewer velocities at the 280 km s^{-1} level. Figure 25 clearly shows proportionally higher velocities for emission-line stars north-east of the main bar and lower velocities south-west of the main bar. This overall gradient is shared by PNe, HII regions and the HI disk but PNe, HII regions and emission-line stars have a greater vertical dispersion at any point than the HI disk.

The common peak velocity ($270 \pm 30\text{ km s}^{-1}$) does not necessarily mean that each population shares the same center of rotation. In fact the rotational centre for PNe and the HI disk have been shown to be located in separate positions (Reid & Parker, 2006b). What we can see from Figure 25 is that $270 \pm 30\text{ km s}^{-1}$ is the average velocity for emission-line stars in the main bar region.

11 DISTRIBUTION ACROSS THE LMC SURVEY AREA

In figure 26 we show the distribution of emission-line stars, superimposed on an $H\alpha$ map of the central 25deg^2 region of the LMC. The surveyed Be stars in the region are shown as filled red circles while M giants are shown as open blue circles.

Much of the resulting distribution depends on our selection criteria since we were searching for compact emission objects and emission stars fainter than $\text{Mag}_R = 14$. For this reason, the most luminous emission-line stars detected in the $H\alpha$ survey were not spectroscopically observed. Objects were selected for spectroscopic follow-up based on the strength of the $H\alpha$ emission relative to the luminosity of the central star. Stars with low ($<5\%$ the central star) $H\alpha$ excess were not spectroscopically followed up as their low variability and/or emission excess over the 3 year duration of the survey indicated that they were not strong emission-line star candidates. Where the criteria were met, we extended the selection to the faintest luminosity candidates we could find. Emission-line stars found in clusters and associations were only earmarked where related velocities or previous published work make the association clear.

The densest distribution of B-F emission-line stars occurs across the main bar. From there they form a line northwards, following the line of nodes (see Reid & Parker 2006b). There is also a large number to be found along the leading arm, south of 30DOR. Being a young population of stars, they trace the more recent star formation regions and HII distribution quite well compared to the older population of PNe, which are more randomly distributed within the LMC (see Reid & Parker 2006b). The somewhat older M population, however, is more evenly distributed across the north and main bar of the LMC. There is a denser distribution of late-type stars along the leading arm which is thought to be a remnant of the LMC's close encounter with the SMC which may have occurred $\sim 2 \times 10^8$ years ago (Murai and Fujimoto, 1980).

12 $H\alpha$ LUMINOSITY EFFECTS AS A FUNCTION OF SPECTRAL TYPE

The theory of equatorial darkening suggests that a degeneracy in the rotational rates allows Be stars to be rotating at or near their critical breakup velocity, Townsend et al. (2004). This implies that there will be a maximum mass and hence, luminosity, allowable for a Be star. The question then arises as to whether the intensity of $H\alpha$ emission from these stars relates to the luminosity class for each star. In other words, does the intensity of $H\alpha$ emission increase in hotter stars? To answer this we have constructed the first ever $H\alpha$ luminosity histogram as a function of spectral type for Be stars, using our sample in the LMC. It is based on measuring the total flux emitted in the $H\alpha$ line over and above the continuum level in each star.

In order to do this, measured $H\alpha$ fluxes were converted to the $H\alpha$ magnitude scale by correlating the $H\alpha$ flux from known emission objects with no continuum and no [N II] contamination against well established $H\alpha$ magnitudes for those objects. A zero point scale was then found in order to convert all $H\alpha$ fluxes to $H\alpha$ magnitudes. This allows comparison to other luminosity functions, such as the planetary nebulae luminosity function, which is already extensively used for distance determination.

This inaugural conversion of $H\alpha$ fluxes to magnitudes was made by choosing PNe with published HST-derived fluxes and 2dF spectra where the PN showed no measurable [N II] $\lambda 6548$ & $\lambda 6583$ but were bright enough to be seen in broad-band R. PNe were chosen because the continuum level is close to zero, allowing the measurement of $H\alpha$ emission only. Each PN was located in the $H\alpha$ map data and an R-band image with an area of 0.1 arcmin radius around each PN was downloaded from SuperCOSMOS online. Along with the image, the IAM data 'tab' file was also downloaded. This file contains precise object positions and R magnitudes from the SuperCOSMOS sky survey and the ESO guide star catalogues. These magnitudes were graphed (see Figure 27) against our calibrated LMC PN fluxes (Reid & Parker 2010) and fluxes from the MCPN catalogue (Stanghellini et al. 2002).

The fit is sufficient to reveal the position of the line of best fit which will be used to perform the conversion. The scatter, up to half a magnitude, seen on either side of the logarithmic line of best fit is to be expected due to the limited linear response of the digitized film and characteristics of the $H\alpha$ filter used on the UKST but does not pose any problem to the calibration of fainter objects since the AB magnitude scale is always fixed at $2.5 \log(F_{H\alpha})$. The logarithmic relation of flux to magnitude means that the slope of the line of best fit will always be fixed. The graph is simply used to attain the magnitude conversion value, which is the final number in the empirical relation:

$$m_{H\alpha} = -2.5 \log F_{H\alpha} - 14.15 \quad (4)$$

for the conversion of all the derived $H\alpha$ fluxes ($\text{ergs}^{-1} \text{cm}^{-2} \text{s}^{-1}$) into $H\alpha$ apparent magnitudes ($m_{H\alpha}$). A mean error estimate of ± 0.27 mag is based on line measurement and flux calibration errors at a total 7% plus 0.1 mag for uncertainties in image photometry.

To check the veracity of this calibration, we used the

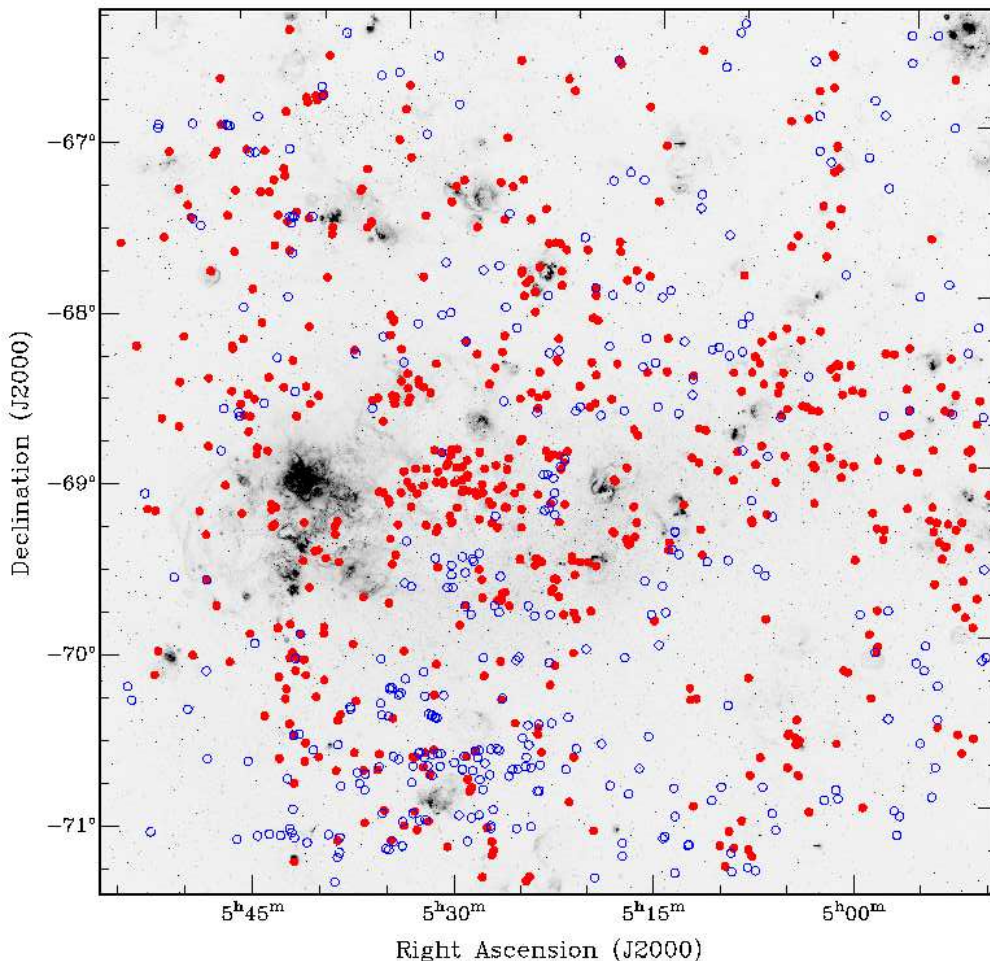


Figure 26. An $H\alpha$ map of the central 25deg^2 region of the LMC showing the distribution of hot emission-line stars as filled red circles. The positions of late-type (mostly M-giant) stars are shown as blue open circles. Stars less than 10 arcsec apart cannot be distinctly separated by the large markers in this image. There is a significant concentration of hot emission-line stars on the immediate north-eastern side of the main bar while M-giants are concentrated to the south.

ESO magnitude-to-flux converter² to convert $H\alpha$ fluxes in $\text{ergs}^{-1} \text{cm}^{-2} \text{s}^{-1}$ to $H\alpha$ magnitudes, using a variety of narrow band filters. Using the accepted flux-to-mag conversion of $-2.5 \log F_{5007} - 13.74$ for $[\text{O III}]\lambda 5007$ emission lines (Jacoby 1989), we simulated a variety of narrow band filters and telescopes and found that any given flux value will be between 0.4 and 0.58 mag brighter in $H\alpha$ than in $[\text{O III}]\lambda 5007$. With our magnitude correction of -14.15, a given flux will be 0.41 mag brighter in $H\alpha$ than in $[\text{O III}]\lambda 5007$, in basic agreement with ESO simulations, giving us added confidence in our new empirical relation.

Using this conversion we constructed the $H\alpha$ luminosity function, which is a measure of the $H\alpha$ emission above the continuum and is presented in terms of the each stars' spectral classification (see Figure 28), a relation which has been unknown to date. The figure shows only a modest increase in $H\alpha$ luminosity with increasing spectral type over a 9 magnitude range. The spectral type or temperature of the star therefore does not correlate strongly with the luminos-

ity of the Balmer emission. As expected, however, classes B0 to B3 dominate the bright end while classes B6 to F9 can mainly be found at the faint end. The bright cutoff occurs at magnitude 15 (an absolute magnitude of -4.5) and the peak in the function (the largest number of stars in any particular bin) occurs at magnitude 18.6. After this peak there is a steady decrease in the distribution over the next 5 magnitudes to the faintest detection at magnitude 23.8. The lone star with a bright $H\alpha$ magnitude of 14.6 is a luminous blue variable (LBV). The shape of the distribution is not unlike that for planetary nebulae in the LMC (see Reid & Parker 2010) but it is unlikely that this function can be used as an extra-galactic distance scale as the brightest $H\alpha$ emission line is a magnitude fainter than the brightest $[\text{O III}]\lambda 5007$ line from PNe in the LMC which is traditionally used for the PNLf.

13 PHOTOMETRY

We obtained B, V, I magnitudes from OGLE-II photometry for 54 previously known Be and B[e] stars which were

² <http://archive.eso.org/apps/mag2flux/>

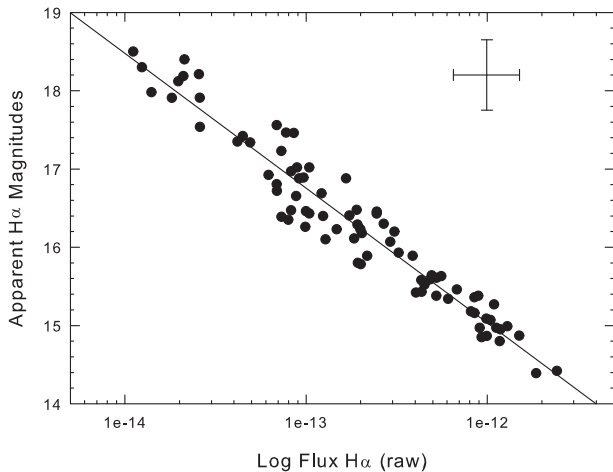


Figure 27. The graph, based on our LMC PN sample, used to convert $H\alpha$ flux to $H\alpha$ magnitude. The apparent $H\alpha$ magnitudes for LMC PNe were measured using image photometry on the stacked $H\alpha$ map. Only PNe with extremely low or no $[N\text{II}]6548$, 6583\AA lines were included in the calibration since the presence of these lines in the wings of the filter can effect the $H\alpha$ measurement. The $H\alpha$ fluxes are from our calibrated 2dF and longslit fluxes for the same PNe. Calibrated this way, there is no need to subtract continuum from the $H\alpha$ line. The scatter is expected due to the limited linear response of the digitised photographic data used to create the $H\alpha$ map. The line of best fit is shown on the graph and the underlying algorithm is provided at equation 4.

found to have strong variability. To this number we add 63 newly discovered Be stars with published OGLE-II photometry (Szymański, 2005, Udalski et al. 2002), found from the limited OGLE coverage of the main bar only. For other stars not in the OGLE data base we gained I, B and R photometry from SuperCOSMOS. The Starlink GAIA image detection option was used to detect and isolate sources by placing an ellipse around the assumed centre. For single stars found in relative isolation this works extremely well. For other sources with close companions or within clusters, the de-blending option was employed. The position of each star was manually checked against the downloaded image to ensure accuracy of positioning and non-blending.

To supplement the OGLE-II V magnitudes we also include GSC2 V magnitudes from ESO. We warn the user to use care in comparing the three photometric sets directly against each other due to intrinsic variability and the change of epoch between the three surveys. Unless specified, we only compare OGLE-II photometry in this section since the published values are an average across the survey period.

13.1 V vs (B-V) colour-magnitude diagram

B stars congregate at the upper left of the traditional H-R colour-magnitude diagram, close to a 0 B-V colour and where the tracks for main sequence, subgiant and giant stars converge. This area of the H-R diagram is a useful test for our Be stars for two reasons. Firstly, by separating giants from main sequence stars, we can independently test our correlated estimates for luminosity class. Secondly, we can

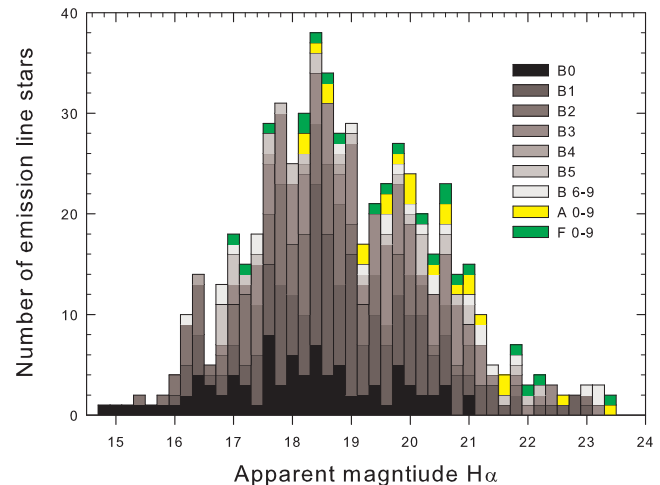


Figure 28. The luminosity function of $H\alpha$ emission from hot emission-line stars found in our survey within the central 25deg^2 region of the LMC. The luminosity bins are 0.2 magnitudes and spectral classifications are indicated in the legend.

see if the variability of these stars is having any effect on the normal position of these stellar classes.

The V versus (B-V) magnitudes for a sample of 100 of our LMC emission-line stars is shown in Figure 29. These magnitudes are derived from OGLE-II photometry where the variability of these stars has been established. Their position on the diagram includes corrections for foreground and intrinsic reddening within the LMC. These reddenings were obtained from the Strömgren CCD photometry on LMC fields conducted by Larsen et al (2000) using B stars. Although several of the stars in this small sample exhibit a strong reddening, only 3 of them - RPs83, RPs1751 and RPs1350 - are visibly surrounded by extended emission halos (≥ 6 arcsec radius). Rather than applying a small reddening to each individual object, we adopt an uncertainty of ± 0.10 for all of these stars since they are close to or on the main bar (Larsen et al. 2000). The stars are separated into main sequence (open red circles) and giants (filled black circles) in Figure 29 where the position of the intrinsic (observed) zero point for (B-V) is shown as a broken vertical line.

The plot indicates that the cross-correlation technique appears to be working very successfully. Main sequence stars appear to be spread across the plot at a broad 45 degree angle from the lower right, following the established track for main sequence stars. Giants on the other hand span across the centre of the plot to the left where they increase in V magnitude.

13.2 $H\alpha$ emission

A correlation has been found between the strength of $H\alpha$ emission and the spatial extent of the emitting region of a Be star (eg. Quirrenbach et al., 1997, Tycner et al. 2005). The $H\alpha$ emission is also thought to be correlated with the observed colour excess (Dachs et al. 1988) where an increase in both $H\alpha$ emission and the colour excess $E(B-V)$ will oc-

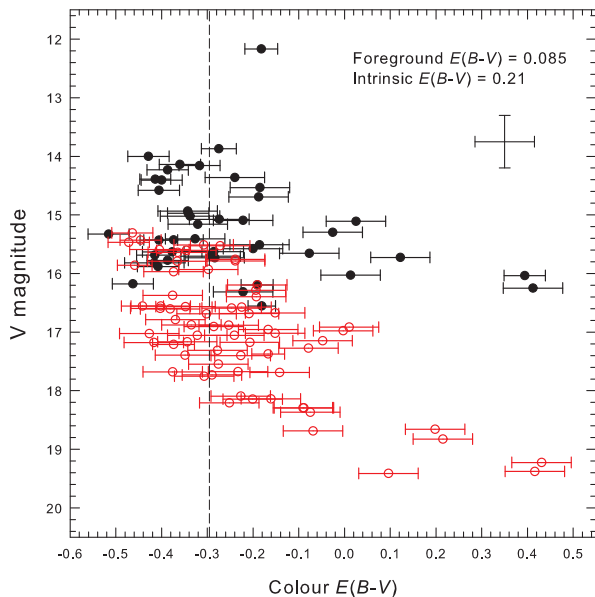


Figure 29. The V versus $E(B-V)$ colour-magnitude diagram from OGLE-II photometry for 117 variable hot emission-line stars found on the LMC main bar. Main sequence stars are assigned red open circles while giant stars are represented by filled black circles. We assume a combined foreground and intrinsic reddening of $E(B-V) = 0.295$. Error bars are based on a combination of B and V published error estimates for B stars on or very close to the main bar. Maximum errors on both scales are shown. The observed position of $(B-V) = 0$ is shown by the broken vertical line.

cur with a larger contribution from bound-free and free-free continuum emission (Beaulieu et al. 2001). For Be stars in our LMC sample, we also find a mild correlation between the Balmer line radiation originating from the stellar envelope as exhibited by $H\alpha$ equivalent width $EW(H\alpha)$ and the $(B-V)$ colour indices. This relation is shown in Figure 30 where the correlation is strongest at low $EW(H\alpha)$.

The increasing scatter with increasing $EW(H\alpha)$ is partly due to increased reddening from interstellar dust and emission from the circumstellar gas envelope, and partly due to complex variations in the $H\alpha$ emission profiles between the time of our spectroscopic observations and the OGLE-II observations. Since the measured $EW(H\alpha)$ is an integrated quantity, it has the tendency to be insensitive to the small-scale variations in the line profile. Effects from OGLE-II photometry, where the LMC was observed repeatedly between 1997 and 2000 will mostly correspond to our 12 $H\alpha$ stacked images, also observed between 1997 and 2000. The average of these photometric variations over 3 year timescales was applied to our spectroscopic observations conducted in 2004 and 2005. Since $(B-V)$ has been averaged out over timescales of years, this ratio is not expected to vary greatly with variation of the star's intrinsic luminosity. For the most variant objects, our spectroscopic measurements of the $H\alpha$ line require slightly larger error margins but re-

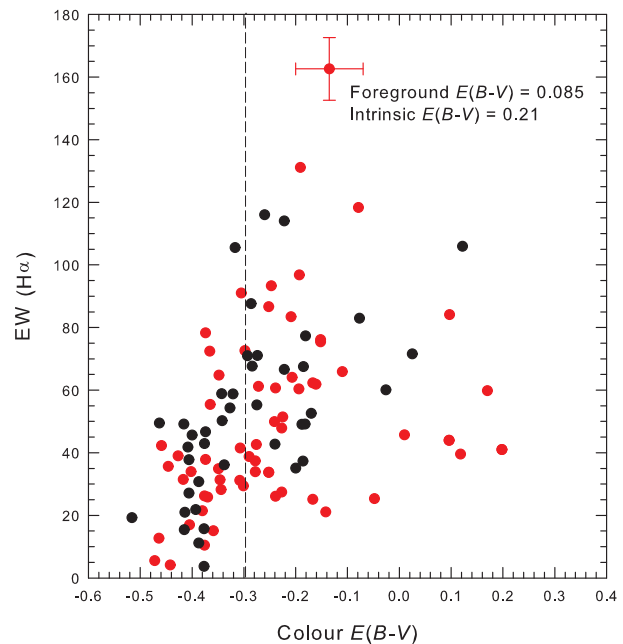


Figure 30. The equivalent width ($H\alpha$) versus $E(B-V)$ colour diagram using our measured $H\alpha$ magnitudes and averaged OGLE-II photometry for 100 variable Be stars in the LMC sample. We assume a combined foreground and intrinsic reddening of $E(B-V) = 0.295$. Error bars are based on a ± 0.10 estimated error for B stars on or very close to the main bar. The observed position of $(B-V) = 0$ is shown by the broken vertical line. There is a mild correlation up to $E(B-V)$ of ~ -0.3 but as the colour index increases the relation breaks down. Giant stars are again shown in black and main-sequence stars are shown in red.

main impossible to estimate without repeated spectroscopic exposures.

Despite these caveats, a mild correlation is still evident. The decrease in the maximum observed value of $(B-V)$ with increasing $EW(H\alpha)$ is one of the main features. It implies that cooler stars will have larger emission shells with a probable maximum size allowable for each spectral class.

In Figure 31 we replace the $EW(H\alpha)$ with the $H\alpha$ emission flux above the continuum. There is no correlation evident, however, the range in $(B-V)$ appears to broaden with decreasing flux suggesting that low $H\alpha$ flux can be present in both the brightest and faintest Be stars.

Figure 32 shows that the $H\alpha$ magnitude is almost consistently fainter than the V magnitude of the star by a mean of 2.72 ± 1 mag. The correlation coefficient between the $H\alpha$ and V magnitudes for our set is only 0.578, implying that the V magnitude of any particular emission-line star could be associated with a wide range of $H\alpha$ flux excess. Figure 32 shows that this could be up to 3 magnitudes either side of the mean correlation, which is $V_{mag} = H\alpha - 2.72$.

The main body of available V magnitudes cease at $V=18$ due to the limit of the ESO catalogue. OGLE-II magnitudes extend to fainter limits. Stars intrinsically fainter than $V=18$ include a wide variety of spectral types so it may be that many of them were undergoing a strong emis-

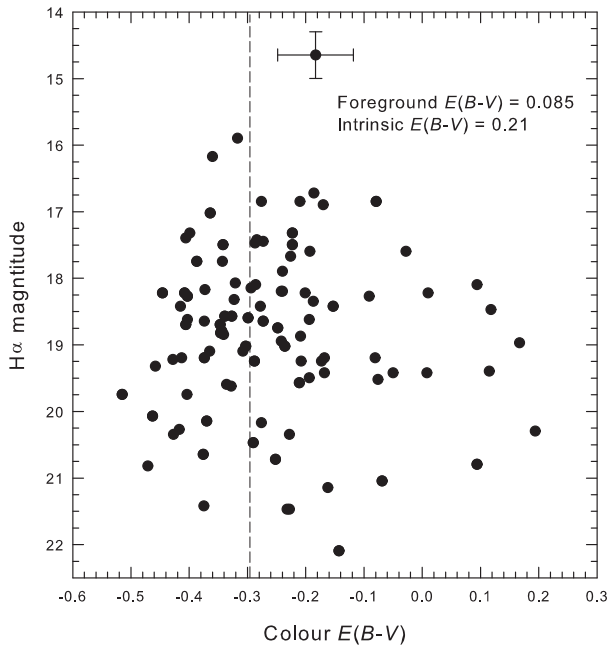


Figure 31. The $H\alpha$ emission from stars in the LMC is compared with their $E(B-V)$ colour. No real correlation between the $H\alpha$ magnitude and colour index can be seen. The magnitude of the $H\alpha$ emission is therefore somewhat independent of the $E(B-V)$ colour of the host star. Similar to Figure 30, however, the minimum observed $E(B-V)$ colour appears to increase with increasing $H\alpha$ magnitude above magnitude 20.

sive phase at the time of our spectroscopic observations. The effect of $H\alpha$ flux variability upon V magnitude is impossible to estimate, however we may assume that a portion of the scatter away from the line of best fit may be due to oscillations.

The emission-line stars in figure 32 have been separated into giants and main sequence classifications in order to investigate their positions on the H-R diagram according to luminosity class. As expected, the giants dominate the bright end and the main sequence stars dominate the faint end of the plot. The overlap region of ~ 2 magnitudes from $V=14.7$ to $V=16.7$ contains about 15 main sequence stars with rather low $H\alpha$ emission. There is nothing peculiar that these stars have in common. Their spectral types range from B1Ve to A6IVe. The size separation either side of the overlap region (V_{mag} 16.7-14.7) is very robust, permitting a secure size assessment to be made based on V magnitude alone.

14 VARIABILITY

The variable nature of Be and B[e] stars is an important feature which relates to the physical stability of the star. As a phenomenon, it has been known for more than a century and may be due to various combinations of physical properties, one or more of which may undergo a transition. Suggested mechanisms are mass loss through stellar winds, rapid ro-

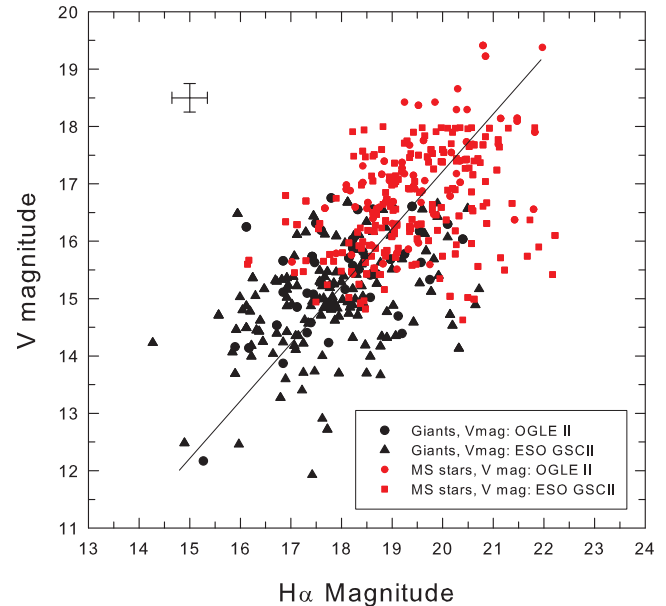


Figure 32. The luminosity of $H\alpha$ emission from stars in the LMC is compared with their V magnitude. Giants and main-sequence stars are separated and assigned black and red colours respectively. A mild correlation can be seen down to the faint cut-off of $V=18$ for the ESO dataset. The linear line of regression indicates that $H\alpha$ magnitudes are generally 2.72 magnitudes fainter than the visual magnitude for these stars. The correlation coefficient is 0.578 and the equation: $V_{mag} = H\alpha - 2.72$, may be used as a rough estimate. Maximum expected errors based on published (for V) and measurement/calibration (for $H\alpha$) are shown.

tation and/or non-radial pulsations (see Porter & Rivinius, 2003). These mechanisms, individually or in combination are usually proposed to explain disc formation and outbursts in Be stars. Sudden brightening and fading episodes are thought to be connected with discrete mass ejection at the surface of Be and B[e] stars. The most notable variations are time dependent variations, known as E/C variations (Hubert-Delplace et al. 1982) where there may be either a change in the emission line intensity or in the continuum level. The latter occasionally cause a veiling effect in the intensity of early-type Be stars.

The jury is still out regarding the mechanism that triggers short-period line profile variability. The possibility of non-radial pulsations has been proposed by several authors (see Rivinius et al. 2003). If the modeling codes (see Townsend, 1997) are observationally confirmed, up to 80% of early-type Be stars may pulsate in one or more modes. Large numbers of spectroscopic observations to detect multi-periodicity will help to decide this issue. Lastly, and related, are the time variations in the intensities of violet and red components (V/R) as seen in double-peaked emission-line profiles. These probably arise from one-armed density waves in the circumstellar disk.

The classification of Be stars in terms of their light curves was initiated by Mennickent et al. (2002) based on their discovery of 1056 Be star candidates in the Small Magellanic Cloud (SMC) using OGLE II data. Having observed

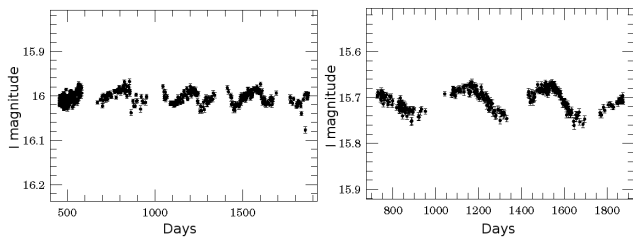


Figure 33. Light curves for RPs1383 (B0Ve, H α : Single Peak, $v \sin i$: $243 \pm 12 \text{ km s}^{-1}$) and RPs1794 (B2V[e], H α : Single Peak, $v \sin i$: $185 \pm 9 \text{ km s}^{-1}$) from the OGLE-II database. These examples show regular variability, with a steady central magnitude.

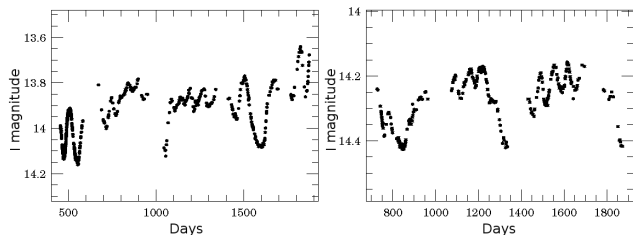


Figure 34. Light curves for RPs870 (B2IV[e], H α : Double Peak R>V, $v \sin i$: $245 \pm 12 \text{ km s}^{-1}$) and RPs2197 (H α : Double Peak R>V, $v \sin i$: $82 \pm 4 \text{ km s}^{-1}$) from the OGLE-II database. These examples show semi-regular variability interspersed with minor variations.

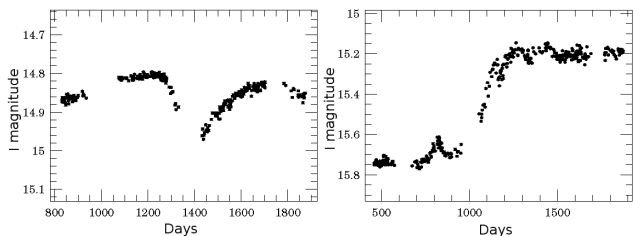


Figure 35. Light curves for RPs1173 (B1IIIe, H α : Single Peak, $v \sin i$: $356 \pm 18 \text{ km s}^{-1}$) and RPs1382 (B1Ve, H α : Double Peak V>R, $v \sin i$: $319 \pm 16 \text{ km s}^{-1}$) from the OGLE-II database. These examples are long period variables which may also include micro features such as that seen at period 1200 days in the right image.

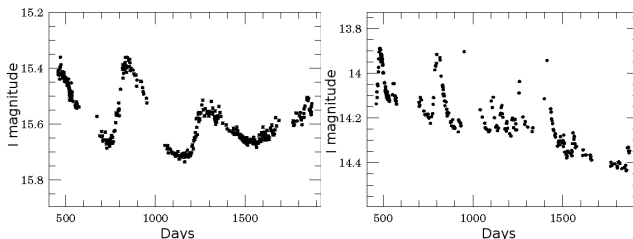


Figure 36. Light curves for RPs1381 (B1Ve, H α : Single Peak, $v \sin i$: $184 \pm 9 \text{ km s}^{-1}$) and RPs1348 (B1IIIe, H α : Single Peak, $v \sin i$: $133 \pm 79 \text{ km s}^{-1}$) from the OGLE-II database. RPs1381 shows quasi-non-regular periods where the brightening can be quite sudden at times. RPs1348 shows semi-regular variability on a broad decline over a long period.

several light curves not seen in Galactic Be stars, they classified four types. Type-1 show outbursts; Type-2 show sudden high and low oscillations; Type-3 show periodic or near periodic variations; Type-4 show the type of light curves seen in Galactic Be stars.

In our data, variability is usually easy to detect by comparing an image taken at a single epoch with our 12 stacked and combined images taken over a 3 year period. While this method strongly indicates variability, the length of the periods can only be measured with repeat exposures over regular intervals.

Although the OGLE photometry currently available does not cover the outer regions of the LMC, there is sufficient data available to find variable stellar candidates within the inner bar region of the LMC. A careful search has found 117 stars with OGLE II data available from our selection of Be stars in the area. Some representative examples of the light curves from these stars are shown in Figures 33 to 36. Periods vary between a few days and over 2,000 days. Magnitude variations range from 0.05 mag (Figure 33 left) to 0.6 mag (Figure 33 right). Many stars show inconsistent variations in both magnitude and period. For example, Figure 34 left shows several 100 day periods followed by a general 0.2 mag increase. The brighter magnitude is accompanied by short bursts which broaden out and increase to 0.3 magnitudes after 900 days. The light curve of RPs1382 (Figure 35 right) shows a short 0.15 mag burst after 400 days (from the start of observations) which precedes and may possibly have pre-cursed a large 0.5 mag increase which was maintained for at least 700 days to the end of the observations. Examples not shown here also include long-term fading episodes such as large decreases over 0.5 in magnitude followed by a wave of short period bursts.

For our LMC data, the larger magnitude variability (>0.2 mag) is mainly confined to early spectral type Be stars (brighter than $\sim B4$). These variations include regular, semi-regular and sporadic outbursts in stars with moderate to high $v \sin i$. Short and mid-term variability on scales of days to weeks can produce amplitudes of up to 0.3 mag. Long-term variability (years to decades) can be accompanied by amplitudes up to 0.8 mag. It is noteworthy that the 2 long period examples with major fading and brightening events shown in Figure 35 have high rotational velocities which are among the highest 20% of $v \sin i$ measurements in our sample.

Figure 36 left shows RPs1381, an example of a Be star which features recurrent outbursts (100 days) which slowly decrease over much longer periods, typically about 400 days in this example. Each outburst has a decreasing amplitude which culminates in a gradual brightening after at least 1000 days.

An interesting phenomenon observed in some variable stars is multiple period oscillations. Low amplitude oscillations are superimposed on much slower and often irregular periods. For example, we find ~ 100 day luminosity bursts or minor periods occurring as stars experience an overall decrease in magnitude lasting in excess of 2000 days (Figure 36 right). The variability of emission-line stars is now recognised as one of the main Be star diagnostics; hence further spectroscopic follow-up has been planned.

15 THE CATALOGUE OF EMISSION-LINE STARS

The full catalogue of emission-line stars uncovered in the stacked $H\alpha$ survey of the central 25deg^2 of the LMC is provided in the Appendix as Tables 1 and 2. In Table 1 we present our measured and derived data whereas in Table 2 we present a compendium of catalogue identifications and magnitudes where available for each star.

In the first column of Table 1 we give the Reid & Parker (RPs) catalogue number where the ‘s’ is added to clearly identify and separate stars from other objects such as PNe, SNRs and H II regions which included in the larger RP catalogue. Columns 2 and 3 give the accurate RA and Dec in J2000 world coordinates to 2 decimal places in RA and 1 decimal place in DEC with reference to SuperCOSMOS and verified against 2MASS astrometry. Column 4 provides a published catalogue reference where a star has been previously identified. Please note that this reference does not necessarily indicate that the star was known as an emission-line star. Column 5 shows our estimate of spectral classification and luminosity class as derived from the cross-correlation described in section 6.1.

Column 6 gives the emission flux from $H\alpha\lambda 6563$ which was measured from our flux-calibrated spectra. All measurements of the $H\alpha$ line including the flux, FWHM (column 7) and the EW (column 8) were measured using the highest quality, medium to high resolution spectra ($R > 1,000$) available in our data set. Individual measurements were made using standard IRAF tasks. The heliocentric velocity shown in column 9 represents the measurement which produced the lowest errors, obtained from our high resolution spectra using the IRAF (EMSAO and XCSAO) tasks. Details are provided in section 10. The estimated rotational velocity ($v \sin i$) is shown in column 10 and described in section 7.

In column 11 we provide comments on each star including a list of which H lines were observed in emission. In the majority of cases, forbidden lines indicate that the star is a B[e] type, however, in several cases, the presence of both low [S II] emission and ambient $H\alpha$ emission (detected in our $H\alpha$ stacked image) suggest that these forbidden lines are not intrinsic to the star itself. In such cases we present the star as a normal Be star but comment on the low [S II] found in the spectrum. Standard abbreviations include ‘SP’ and ‘DP’ indicating an $H\alpha$ line with a single peak or a double peak respectively. The ‘DP’ abbreviation is usually followed by either ‘V>R’, ‘R>V’, or ‘centre’ indicating the position of the absorption feature (see section 6.4).

The second table presented in the appendix contains a compilation of the B, V, I and R photometry available for each object in this work. In the first three columns we again provide the RP number, RA and DEC of each object to make identification and cross-referencing easier. The fourth column lists the GSC2.2 catalog reference number while column 5 gives the linear distance in arcmins between our position and the GSC2.2 position. Positional errors at the plate epoch are estimated to be in the 200-250 mas range. Column 6 gives the OGLE catalog reference where the matching position has been found in the OGLE II database. Column 7 gives the USNO-A2.0 catalog reference with the linear distance in arcmins between our position and the best matching USNO position shown in column 8. It is estimated that the

positional error at plate epoch is near 250 mas. Column 9 then provides the position angle (PA) for each object published in the USNO catalog.

The remaining columns, 10 to 18 provide the magnitudes where available for each star. Since emission-line stars are variable, we should expect a comparison of surveys to reveal minor variations in overall flux estimates. These modulations are confirmed by the data presented here.

In columns 10 to 12 we present the B magnitudes from OGLE, SuperCosmos (SC) and USNO respectively. Columns 13 and 14 give the V magnitudes from GSC2.2 and OGLE. Columns 15 and 16 give the I magnitudes from SC and OGLE and columns 17 and 18 give the R magnitudes from SC and USNO.

Our online database to be hosted at Macquarie University will contain extra information relating to each star. We will provide optical spectra for each object as well as 1×1 arcmin $H\alpha$ /Short Red thumbnail images. At the time of writing, the web site is under construction.

16 SUMMARY

Using our deep $H\alpha$ and SR maps centered on the central 25deg^2 of the LMC, we have uncovered 1,003 stars which exhibit $H\alpha$ emission. A series of follow-up spectroscopic observations were performed, mostly using 2dF on the AAT during December 2004. The majority of the stars have been assigned a spectral classification using the IRAF cross-correlation technique and spectral class templates. In addition to the 111 previously known Be stars we have added 468 newly discovered Be, B[e], A and F stars. Most of these stars fall between spectral classes B1 and B3. Analysis of the survey data has also allowed us to identify 315 M (late-type) stars exhibiting chromospheric emission.

For the hot emission-line stars, we provide new, accurate positions, radial and rotational velocities. The distribution of radial velocities has been plotted and compared to the heliocentric distributions for PNe and the H I gas disk in the LMC. The good agreement not only indicates that all our emission-line star candidates are located in the LMC, but traces the overall inclination of the LMC’s main disk. The distribution of rotational velocities has been plotted and compared to a Galactic sample, revealing a 200-300 km s^{-1} agreement in the peak of the distributions. We have also briefly discussed the various $H\alpha$ emission-line profiles identified in our LMC sample.

Emission from the hot B to F stars has been measured and flux calibrated in order to provide the first ever luminosity function for the $H\alpha$ emission from these stars. This included the first ever derived conversion from $H\alpha$ fluxes to magnitudes, with its associated formula, which can be used generally for emission objects in the LMC. The emission has a bright cut-off at magnitude 14.8 (absolute -4.5) and covers a 9 magnitude range. The function shows a steady rise to a distribution peak at 18.5 followed by a decrease over 5 magnitudes to magnitude 23.6. We find a mild correlation between the $H\alpha$ and V magnitudes of the hot stars in our sample. Main sequence stars in our sample are only found at magnitudes below 14.5 in V whereas giants extend to magnitude 12 in V. A compilation of B,V,I and R magnitudes

from OGLE II, SuperCOSMOS, ESO GSC 2.2 and USNO are provided in Table 2 of the Appendix.

A plot of the distribution of emission-line stars within the survey area shows that approximately 40% lie on the main bar. As many as 130 (25%) of the B-class stars are found to be of the B[e] variety, emitting forbidden lines in [S II], [N II], [O I] and even [O III]. Many of these are located in areas of strong ambient emission or H II regions so care is needed to removed these contributions if only emission associated with or emitting from the star is to be measured. These stars with probable contamination have been labeled accordingly within the tables.

17 ACKNOWLEDGEMENTS

The authors wish to thank the AAO board for observing time on the AAT and UKST. The authors also thank the European Southern Observatory for observing time on the VLT and Australian National University along with their telescope time allocation committees for supporting our programme of follow-up spectroscopy. We thank the anonymous referee for very helpful comments and suggestions while carefully reviewing the paper. Lastly we would like to thank Suzanne Reid from Kalidus Systems for lending her database design skills to create a repository for the emission-line star data.

REFERENCES

- Acke B., van den Ancker M.E., Dullemond C.P. 2005, *A&A*, 436, 209
- Andrews A.D., Lindsay E.M., 1964, *IrAJ*, 6, 241
- Andrillat Y., & Houziaux L. 1991, *IAUC*, 5164, 3
- Beaulieu J-P., et al., 2001, *A&A* 380, 168
- Bohannan B.E., Epps H.W., 1974, *A&AS*, 18, 47
- Böhm T., & Catala C. 1994, *A&A*, 290, 167
- Böhm T., & Hirth G.A. 1997, *A&A*, 324, 177
- Bowyer S., Sasseen T.P., Wu X., Lampton M., 1995, *AJ* suppl. ser. 96, 461
- Bjorkman J.E., Cassinelli J.P., 1993, *ApJ*, 409, 429
- Bjorkman K. S., Miroshnichenko A.S., McDavid D., Pogrosheva T.M. 2002 *ApJ*, 573, 812
- Bland-Hawthorn J., Shopbell P.L., Malin D., 1993, *AJ*, 106, 2154B
- Butler C.J., Wayman P.A., 1974, *DunOP*, 1, 193
- Cassinelli J.P., Brown J.C., Maheswaran M., Miller N.A., Telfer D.C., 2002, *ApJ*, 578, 951
- Cohen M., Kuhl L., 1979, *ApJS*, 41, 743
- Corcoran M., Ray T.P., 1998 *A&A*, 331, 147
- Cranmer S.R., 2005, *ApJ*, 634, 585
- Dachs J., Hanuschik R.W., Kaiser D., & Rohe D., 1986, *AA*, 159, 276
- Dachs J., Kiehling R., Engels D., 1988, *A&A*, 194, 167
- Draper H., 1924, *Ann. Astron. Obs. Harvard* 91-100, 1-6
- Feast M. W.; Thackeray, A. D.; Wesselink, A. J. 1960, *MNRAS* 121, 337
- Frew D., Parker Q., 2010, *PASA*, 27, 129
- Gordon K.D., Clayton G.C., Misselt K.A., Landolt A.U., Wolff M.J., 2003, *ApJ*, 594, 279
- Grebel E.K., 1997, *A&A*, 317, 448
- Grebel E.K., Chu Y., 2000, *AJ*, 199, 787
- Gullbring E., Hartmann L., Briceno C., Calvet N., 1998, *ApJ*, 492, 323
- Hamann F., 1994, *ApJS*, 93, 485
- Hambly N. C., et al., 2001, *MNRAS*, 326, 1279H
- Hanuschik R.W., 1989, *Ap&SS*, 161, 61
- Hanuschik R.W., Hummel W., Sutorius E., Dietle O., Thimm G., 1996, *A&AS*, 116, 309
- Hartigan P., Edwards S., Ghandour L., 1995, *ApJ*, 452, 736
- Hartmann L., Hewett R., Calvet N., 1994, *ApJ*, 426, 669
- Heney L.G., Lelevier R., Levée R.D., 1955, *PASP* 67, 154
- Henize K.G., 1956, *ApJS*, 2, 315
- Hubert-Delplace A. M., Hubert H., Chambon M. T., Jaschek M. 1982 *IAUS: Be stars; Proceedings of the Symposium, Munich, West Germany, 1981, Dordrecht, D. Reidel*, 98, 125
- Hubert A.M., Floquet M., 1998, *A&A*, 335, 565
- Herbig G.H., 1960, *ApJS*, 4, 337
- Hernández J., Calvet N., Briceño C., Hartmann L., Berlind P., 2004, *AJ*127, 1682
- Hillenbrand L.A., Strom S.E., Vrba F.J., Keene J., 1992, *ApJ*, 397, 613
- Hubrig S., Schöller M., Yudin R.V. 2004, *A&A*, 428, L1
- Hughes S.M.G., 1989, 97, 1634
- Hummel W., Szeifert T., Gässler W., Muschielok B., Seifert W., Appenzeller I., Rupprecht G., 1999 *A&A* 352, L31
- Hutsemékers D. 1985, *A&AS*, 60, 373
- Jaschek M., Jaschek C., 1967, *ApJ*, 150, 355
- Jacoby G.H., Hunter, D.A., Christian C.A., 1984, *ApJS*, 56, 257
- Jacoby G.H., 1989. Planetary nebulae as standard candles. I. Evolutionary models. *ApJ*, 339, 39
- Jaschek M., Jaschek C., 1967, *ApJ*, 150, 355
- Jaschek M., Slettebak A., Jaschek C., 1981 *Be Star Newsl.*, 4, 9
- Kaler J.B., 1997, *Stars and their spectra*, Univ. press Cambridge. ISBN 0 521585708 p 192
- Keller S.C., Wood P.R., Bessell M.S., 1999, *A&AS*, 134, 489
- Keller S.C., Bessell M.S., Da Costa G.S., 2000, *AJ*, 119, 1748
- Keller S.C., Bessell M.S., Cook K. H., Geha M., Syphers D., 2002, *AJ*, 124, 2039
- Königl A., 1991, *ApJ*, 370, L39
- Kontizas E., Dapergolas A., Morgan D. H., Kontizas M., 2001, *A&A*, 369, 932
- Kurtz M.J., Mink D.J., 1998, *PASP*, 110, 934
- Lada C.J., Adams F.C., 1992, *ApJ*, 393, 278
- Larsen S.S., Clausen J.V., Storm J., 2000, *A&A*, 364, 455
- Le Borgne J.-F., Bruzual G., Pelló R., Lançon A., Rocca-Volmerange B., Sanahuja B., Schaerer D., Soubiran C., Vílchez-Gómez R., 2003, *A&A* 402, 433
- Lewis I.J., et al., 2002, *MNRAS*, 333, 279
- Lindsay E.M., 1963, *IrAJ*, 6, 127
- Lindsay E.M., 1974, *MNRAS* 166, 703
- Lumb D.H., Guainazzi M., Gondoin P., 2001, *A&A*, 376, 387
- Melchior A.-L., Hughes S. M. G., Guibert J., 2000, *A&AS*, 145, 11
- Mennickent R.E., Pietrzyński G., Gieren W., Szewczyk O., 2002, *A&A*, 393, 887

- Miroshnichenko A.S., Fabregat J., Bjorkman K.S., Knauth D.C., Morrison N.D., Tarasov A.E., Reig P., Negueruela I., Blay P., 2001, *A&A*, 371, 600
- Morgan W. W., Keenan P.C., Kellman E. 1943, “An atlas of stellar spectra, with an outline of spectral classification”, Chicago, Ill., The University of Chicago press
- Murai T., Fujimoto M., 1980, *PASJ*, 32, 581
- Muzerolle J., Calvet N., Hartmann L., 1998, *ApJ*, 492, 743
- Muzerolle J., Calvet N., Hartmann L., 2001, *ApJ*, 550, 944
- Muzerolle J., D’Alessio P., Calvet N., Hartmann L., 2004, *ApJ*, 617, 406
- Olsen K.A.G., Kim S., Buss J.F., 2001 *AJ*, 121, 3075
- Parker Q.A., Bland-Hawthorn J., 1998, *PASA*, 15, 33p
- Parker Q.A., Malin D., 1999, *PASA*, 16, 288P
- Parker Q.A., et al., 2005 *MNRAS* 362, 689
- Pasquini L., et al., 2002, *Msngr.* 110, 1
- Poeckert R., Marlborough J.M., 1978, *A.J.suppl.* 38, 229
- Porter J.M., 1996, *MNRAS*, 280, 31
- Porter J.M., Rivinius T., 2003 *PASP*, 115, 1153
- Pickles A.J., 1998, *PASP*, 110, 863
- Quirrenbach A., Bjorkman K.S., Bjorkman J.E., Hummel C.A., Buscher D.F., Armstrong J.T., Mozurkewich D., Elias N.M.II, Babler B.L., 1997, *ApJ*, 479, 477
- Reid N., Glass I.S., Catchpole R.M., 1988, *MNRAS*, 232, 53
- Reid W.A., Parker Q.A. 2005, *AIPC*, 804, 12
- Reid W.A., Parker Q.A. 2006a, *MNRAS*, 365, 401
- Reid W.A., Parker Q.A. 2006b, *MNRAS*, 373, 521
- Reid W.A., Parker Q.A. 2010, *MNRAS*, 405, 1349
- Rivinius Th., Baade D., Štefl S., Townsend R.H.D., Stahl O., Wolf B., Kaufer A., 2001, *A&A*, 369, 1058
- Rivinius Th., Baade D., Štefl S., 2003, *A&A*, 411, 229
- Rohlfs K., Kreitschmann J., Feitzinger J.V., Siegman B.C., 1984, *A&A*, 137, 343
- Sabogal B.E., Mennickent R.E., Pietrzyński G., Gieren W., 2005, *MNRAS*, 361, 1055
- Schwering P.B.W., 1989, *A&A Suppl. Ser.* 79, 105
- Silaj J., Jones C.E., Tycner C., Sigut T.A.A., Smith A.D., 2010, *ApJS*, 187, 228
- Silva D.R., Cornell M.E., 1992, *ApJS*, 81, 865
- Skrutskie M.F., et al., 2006, *AJ.*, 131, 1163
- Slettebak A., 1982, *AJ. Supp. Series*, 50, 55
- Stanghellini L., Shaw R.A., Mutchler M., Palen S., Balick B., Blades J.C., 2002, *ApJ*, 575, 178
- Struve O., 1931, *ApJ*, 73, 94
- Szymański M.K., 2005, *Acta Astron.*, 55, 43
- Telting J.H., 2000 in *ASP Conf. Proc.* 214, The Be Phenomenon in Early-Type Stars, ed. M.A. Smith & H.F. Henrichs (San Francisco: ASP), 422
- Tonry J.L., Davis M., 1979, *AJ.* 43, 393
- Townsend R.H.D., 1997, *MNRAS*, 284, 839
- Townsend R.H.D., Owocki S.P., Howarth I.D., 2004, *MNRAS*, 350, 189
- Turnshek D.E., Turnshek D.A., Craine E.R., Boeshaar, P.C., 1985, *An atlas of digital spectra of cool stars* Astronomy and Astrophysics Series, v.1, Tucson: Western Research Company, ISBN 0-934525-00-5
- Tycner C., et al., 2005, *ApJ*, 624, 359
- Uchida Y., Shibata K., 1985, *PASJ*, 37, 515
- Udalski A., Szymański M., Kubiak M., Pietrzyński G., Soszyński I., Woźniak P., and Zebruń K., 2000, *Acta Astron.*, 50, 307
- Underhill A., Doazan V., 1982, “B STARS with and without emission” NASA SP-456, Washington DC.: NASA
- Van Winckel H., 2003, *ARA&A*, 41, 391
- Viera S.L.A., Corradi W.J.B., Alencar S.H.P., Mendes L.T.S., Torres C.A.O., Quast G.R., Guimarães M.M., da Silva L. 2003, *AJ*, 126, 2971
- Waters L.B.F.M., Waelkens C., 1998, *ARA&A*, 36, 233
- Wade G.A. et al., 2005, *A&A*, 442, L31
- Wisniewski J.P., Bjorkman K.S., 2006 *ApJ*, 652, 458

This paper has been typeset from a \TeX / \LaTeX file prepared by the author.

1 APPENDIX: TABLE 1

Basic data for all hot emission-line stars in the LMC UKST H α survey. Please refer to section 15 for more detailed information. Column 1 gives the Reid Parker (RPs) number for the star (s). Columns 2 and 3 give the RA and Dec in J2000 coordinates. Column 4 gives the published catalogue and number where a star has been previously identified. Column 5 gives our estimate of spectral classification and luminosity class. Column 6 gives a log of the H α emission flux obtained from our flux calibrated spectra. Column 7 gives the Full Width at Half Maximum (FWHM) in km/s as measured from our data. Column 8 gives the Equivalent Width (EW) of the H α line in Angstroms. Column 9 gives the heliocentric radial velocity and column 10 gives the rotational velocity ($v \sin i$). In column 11 we provide comments where em=emission, A.Em=ambient emission, SP=single peak, DP=double peak, sh=shell. Notes on column 4 are given at the end of the table.

RP Object	RA J2000	DEC J2000	Other Catalog Reference	Spec Type	Log F H α	FWHM H α km/s	EW H α Å	Vel. (helio) km/s	$v \sin i$ km/s	Comments
RP1741	04 52 55.41	-70 42 12.3		B7Ve	-13.92	464 ± 23	70 ± 3	326 ± 6	449 ± 22	H α , β
RP1647	04 53 01.03	-70 42 12.3		B3Ve	-13.97	342 ± 17	18 ± 1	241 ± 1	243 ± 12	H α , [S II] from faint, diffuse local emission
RP1701	04 53 02.01	-69 47 04.1		B2Ve	-13.73	333 ± 17	55 ± 2	236 ± 5	296 ± 15	H α , β
RP1699	04 53 06.86	-69 57 24.7		B1.7V[e]	-13.33	56 ± 3	59 ± 2	242 ± 1	22 ± 1	H α , β , γ , [S II], [N II], [O II]
RP1671	04 53 25.43	-70 35 39.7		B0III[e]	-12.78	247 ± 12	19 ± 1	262 ± 1	165 ± 8	H α , β , γ , [S II], [N II], [O III]
RP1778	04 53 43.26	-69 54 02.3		B2Ve	-13.18	282 ± 14	74 ± 3	271 ± 4	267 ± 13	H α , β
RP1715	04 53 54.12	-69 29 24.9		B1.5Ve	-13.64	349 ± 17	48 ± 2	260 ± 4	304 ± 15	H α , β
RP1704	04 54 06.45	-69 41 14.9		B1Ve	-13.36	362 ± 18	77 ± 3	261 ± 5	352 ± 18	H α , β
RP1844	04 54 08.72	-68 37 02.9		B3IIIe	-12.88	307 ± 15	61 ± 2	289 ± 4	278 ± 14	H α , β
RP1757	04 54 11.97	-69 00 53.9	BE74162	B1Ve	-13.29	357 ± 18	89 ± 4	275 ± 5	356 ± 18	H α , β
RP1814	04 54 12.32	-68 45 21.0		B2Ve	-13.84	345 ± 17	44 ± 2	253 ± 5	300 ± 15	H α , β
RP1700	04 54 23.92	-69 50 53.2		B1Ve	-13.20	336 ± 17	56 ± 2	238 ± 5	299 ± 15	H α , β
RP1767	04 54 26.05	-68 54 38.1		B3Ve	-13.36	260 ± 13	30 ± 1	286 ± 4	199 ± 10	H α , Pcyg. Profile on H β
RP1765	04 54 30.18	-68 55 25.2		B2Ve	-13.49	317 ± 16	40 ± 2	302 ± 5	264 ± 13	H α , β
RP1783	04 54 33.88	-69 20 35.7	L6331	B2III[e]	-12.40	129 ± 6	113 ± 5	240 ± 3	116 ± 6	H α , β , γ , δ , multiple forbidden lines. Few absorption lines. Weak correlation.
RP1766	04 54 37.11	-68 55 19.4		B2Ve	-13.62	250 ± 12	42 ± 2	280 ± 12	201 ± 10	H α , β
RP1784	04 54 53.95	-69 23 23.7		B0Ve	-13.08	100 ± 5	69 ± 3	277 ± 23	70 ± 4	H α , β , in area of strong H α emission 20 x 16 arcsec with filament to NE
RP1651	04 54 54.76	-70 33 41.4		B2IIIe	-12.87	325 ± 16	78 ± 3	233 ± 5	313 ± 16	H α , β , γ
RP1781	04 55 27.18	-69 29 33.1		B2Ve	-13.07	175 ± 9	41 ± 2	254 ± 3	130 ± 7	H α , β
RP1786	04 55 28.71	-69 21 36.5		B3IIIe	-12.57	283 ± 14	68 ± 3	253 ± 4	260 ± 13	H α , β
RP1780	04 55 33.97	-69 29 43.5		B2IIIe	-12.58	343 ± 17	49 ± 2	267 ± 5	298 ± 15	H α , β
RP1710	04 55 39.89	-69 34 09.0	L6339	B3III	-12.76	336 ± 17	45 ± 2	255 ± 4	291 ± 15	H α , β , patchy emission in local area
RP1843	04 55 44.36	-68 35 42.9		B1III[e]	-12.91	57 ± 3	80 ± 3	275 ± 2	27 ± 1	H α , β , [S II], [N II], centre of complex, dense stellar cluster 19 arcsec dia with strong H α emission surrounding all.
RP1779	04 55 58.23	-69 28 18.3	MACHO17.2472.36	B1III[e]	-13.02	192 ± 10	25 ± 1	261 ± 3	128 ± 6	H α , β , faint and diffuse emission in area contributes [S II], [N II], [O II] and [O III] at low levels.
RP1829	04 55 59.94	-68 42 08.8		B2IVe	-13.97	260 ± 13	43 ± 2	308 ± 4	211 ± 11	H α , β
RP1703	04 56 01.98	-69 43 22.8	MACHO17.2468.63	B1Ve	-13.10	300 ± 15	56 ± 2	253 ± 4	271 ± 14	H α , β
RP1733	04 56 14.22	-69 21 29.6		B3IIIe	-12.80	371 ± 19	100 ± 4	274 ± 5	382 ± 19	H α , β
RP1857	04 56 14.37	-68 22 59.3		B3IIIe	-12.86	322 ± 16	56 ± 2	282 ± 5	293 ± 15	H α , β
RP1828	04 56 23.14	-68 41 34.4		B5IIIe	-13.81	288 ± 14	49 ± 2	311 ± 4	244 ± 12	H α , (Pcyg profile on H β)
RP1782	04 56 23.42	-69 24 41.5		B2IV[e]	-13.18	56 ± 3	175 ± 7	253 ± 1	41 ± 2	H α , β , γ , δ , ϵ , [S II], [N II], [O II], [O III]
RP1736	04 56 37.52	-69 16 08.5		B1Ve	-13.28	351 ± 18	44 ± 2	242 ± 5	306 ± 15	H α , β
RP1732	04 56 44.68	-69 20 53.4		A5Ve	-13.72	147 ± 7	32 ± 1	253 ± 3	96 ± 5	H α , β
RP1762	04 56 54.26	-68 55 54.6		F8Ve	-13.48	237 ± 12	24 ± 1	291 ± 4	167 ± 8	H β line suffers from low S/N
RP1928	04 57 26.91	-66 44 08.7		B3V[e]	-14.49	307 ± 15	83 ± 3	304 ± 40	302 ± 15	H α , β , [S II], [N II], [O II], [O III], emission to East, star to West
RP1746	04 57 48.54	-69 04 15.6		B3Ve	-13.91	329 ± 16	43 ± 2	276 ± 3	276 ± 14	H α , β , ([S II] at 2 σ noise)
RP1884	04 58 07.26	-67 41 11.4		B0.5II[e]	-12.26	100 ± 5	125 ± 5	301 ± 21	86 ± 4	H α , β , γ , [S II], [N II], [O II], [O III]
RP1737	04 58 17.48	-69 17 20.1		B1.7Ve	-13.68	333 ± 17	48 ± 2	288 ± 4	288 ± 14	H α , β
RP1806	04 58 33.31	-68 50 49.9	HD268840	B0.5III[e]	-11.69	286 ± 14	71 ± 3	279 ± 4	264 ± 13	H α , β , γ , δ , ϵ , [S II], [N II], [O II], [O III]
RP1826	04 58 38.12	-68 42 26.5		B2IV[e]	-13.32	441 ± 22	45 ± 2	299 ± 9	393 ± 20	H α , β , [O III]
RP1804	04 58 55.65	-68 51 45.1		B3IIIe	-12.84	408 ± 20	36 ± 1	284 ± 6	342 ± 17	H α , β
RP1747	04 58 56.23	-69 03 29.1		F8II[e]	-12.65	212 ± 11	76 ± 3	294 ± 3	193 ± 10	H α , β , γ , δ , low [O III], HeII 4686, [S II], [N II]
RP1839	04 58 56.52	-68 35 02.8	MACHO18.3090.104	B5IIIe	-12.76	188 ± 9	50 ± 2	262 ± 3	151 ± 8	H α , β , Could appear as a B8 I star
RP1860	04 58 58.47	-68 20 32.8		B3IIIe	-13.33	266 ± 13	72 ± 3	245 ± 4	250 ± 13	H α , β
RP1774	04 59 35.00	-70 06 59.0		B1V[e]	-13.25	339 ± 17	33 ± 1	231 ± 1	270 ± 14	H α , Pcyg on H β , [S II], [N II], [O II]. East star of double system
RP1775	04 59 37.18	-70 09 09.6	BE74499	B0.5II[e]	-12.59	49 ± 2	109 ± 4	235 ± 1	24 ± 1	H α , β , γ , δ , [S II], [N II], [O II], dense H II disk extending to 2 smaller stars to the SE
RP1717	04 59 44.89	-69 28 57.2		B0Ve	-13.13	309 ± 15	32 ± 1	259 ± 4	243 ± 12	H α , β
RP1724	04 59 44.90	-69 25 32.5		B3Ve	-13.06	229 ± 11	68 ± 3	261 ± 3	204 ± 10	H α , β

RP Object	RA J2000	DEC J2000	Other Catalog Reference	Spec Type	Log F H α	FWHM H α km/s	EW H α Å	Vel. (helio) km/s	$v \sin i$ km/s	Comments
RP s1656	04 59 46.62	-70 25 27.7		B1Ve	-13.74	509 ± 25	60 ± 2	278 ± 9	483 ± 24	H α only, Pcyg on H β
RP s1698	04 59 48.42	-69 54 13.0	L6370	B1Ve	-12.99	290 ± 14	78 ± 3	226 ± 4	276 ± 14	H α, β
RP s1856	04 59 54.75	-68 23 07.4		B0.5IIIe	-13.16	410 ± 20	50 ± 2	289 ± 6	373 ± 19	H α, β, γ
RP s1777	05 00 13.12	-70 02 56.5	SVDV 284	B1.5Ve	-13.56	291 ± 15	79 ± 3	246 ± 4	277 ± 14	H α, β
RP s1722	05 00 14.06	-69 25 13.9	SAB2338	B2Ve	-13.01	309 ± 15	61 ± 2	250 ± 4	280 ± 14	H α, β
RP s1855	05 00 28.46	-68 23 04.4		B2Ve	-13.56	547 ± 27	41 ± 2	274 ± 9	483 ± 24	H α, β
RP s1755	05 00 28.77	-69 01 06.3	SAB1539	B3Ve	-13.23	323 ± 16	77 ± 3	277 ± 5	310 ± 16	H α, β
RP s1729	05 00 35.39	-69 19 53.3	SAB744	B3IIIe	-13.16	272 ± 14	50 ± 2	272 ± 4	235 ± 12	H α, β
RP s1662	05 01 32.53	-70 16 56.1	MACHO23.3428.997	B1Ve	-13.28	477 ± 24	54 ± 2	251 ± 6	439 ± 22	H α, β
RP s1707	05 01 33.25	-69 36 58.7		B1Ve	-12.79	353 ± 18	106 ± 4	274 ± 5	372 ± 19	H α, β
RP s1832	05 01 48.92	-68 37 33.6	SAB1625	B3IIIe	-13.00	347 ± 17	56 ± 2	238 ± 5	319 ± 16	H α, β, γ
RP s1663	05 01 50.52	-70 16 14.9		B2Ve	-13.65	363 ± 18	66 ± 3	261 ± 4	344 ± 17	H α, β
RP s1645	05 02 00.95	-70 42 23.7	BE74504	B1V[e]	-12.70	90 ± 5	106 ± 4	254 ± 2	71 ± 4	H α, β , [S II], [N II], [O II] (emission lines brighter than continuum).
RP s1792	05 02 03.12	-68 03 40.9	SAB1656	B0V[e]	-13.28	247 ± 12	43 ± 2	271 ± 3	198 ± 10	H α, β , [S II], [N II], [O II]
RP s1838	05 02 26.96	-68 36 55.8	AL56	BIIIpe	-12.09	281 ± 14	86 ± 3	292 ± 4	274 ± 14	H α, β equal to a B2IIIe
RP s1854	05 02 39.99	-68 27 59.4		B1.7V[e]	-12.70	56 ± 3	140 ± 6	286 ± 2	37 ± 2	H α, β, γ , [S II], [N II], [O II], within a small assoc. of stars.
RP s1750	05 02 45.65	-69 03 13.1		B1V[e]	-13.65	77 ± 4	18 ± 1	287 ± 2	23 ± 1	H α, β , [S II], [N II]
RP s1745	05 02 50.69	-69 07 57.6	SAB236	B1.7Ve	-14.30	95 ± 5	11 ± 0	285 ± 2	29 ± 1	H α , (H β with strong Pcyg profile.) Forbidden lines and 40% H α due to diffuse emission 20 arcsec diameter stretching NE-SW
RP s1834	05 03 04.89	-68 38 35.6		B3Ve	-13.96	234 ± 12	44 ± 2	274 ± 3	191 ± 10	H α , (Pcyg profile on H β)
RP s1850	05 03 26.01	-68 28 24.3		F0Ive	-13.80	471 ± 24	146 ± 6	199 ± 12	533 ± 27	H α, β , weak continuum
RP s1852	05 03 32.09	-68 27 56.1		B1Ve	-14.23	315 ± 16	33 ± 1	285 ± 15	249 ± 12	H α, β , ([S II] appears to be assoc. with emission to NW)
RP s1845	05 03 32.94	-68 32 35.0		B1Ve	-14.62	296 ± 15	5 ± 0	272 ± 1	146 ± 7	H α only. Centre of faint, extended H II emission 12 x 12 arcsec.
RP s1794	05 03 38.63	-69 01 21.2	SAB839	B2V[e]	-13.17	239 ± 12	37 ± 1	278 ± 3	185 ± 9	H α, β , [S II], [N II], [O III], SP
RP s1793	05 03 38.94	-69 01 11.9		B1Ve	-13.76	203 ± 10	29 ± 1	283 ± 1	142 ± 7	H α , pcyg profile on H β , [S II] from local diffuse nebula
RP s1851	05 03 39.12	-68 28 23.7		B1Ve	-14.40	291 ± 15	5 ± 0	286 ± 1	143 ± 7	H α , [S II] at only 3 σ noise
RP s1614	05 03 41.74	-71 07 09.7		A7Ve	-14.36	198 ± 10	46 ± 2	235 ± 2	156 ± 8	H α
RP s1760	05 03 51.47	-68 57 25.3	BE74193	B1IIIe	-13.42	733 ± 37	17 ± 1	233 ± 24	553 ± 28	H α, β, γ , [S II]
RP s1899	05 03 52.12	-67 32 43.6		A0Ve	-13.45	207 ± 10	61 ± 2	282 ± 15	176 ± 9	H α, β
RP s1945	05 04 09.07	-67 18 30.1		B2IIIe	-12.58	424 ± 21	32 ± 1	308 ± 6	347 ± 17	H α, β
RP s1910	05 04 17.16	-67 10 55.4		B0IIIe	-13.69	192 ± 10	38 ± 2	290 ± 6	142 ± 7	H α, β , [S II]
RP s1909	05 04 18.26	-67 10 30.3		B3IIIe	-13.59	97 ± 5	20 ± 1	297 ± 17	41 ± 2	H α , [S II]
RP s1944	05 04 24.06	-67 19 45.9		B2V[e]	-13.43	259 ± 13	73 ± 3	306 ± 23	243 ± 12	H α, β, γ , [S II], [N II], [O II], [O III]
RP s1738	05 04 31.78	-69 17 40.9		B8Ve	-14.19	382 ± 19	22 ± 1	286 ± 5	285 ± 14	H α
RP s1817	05 04 35.61	-68 44 55.1	AL66	F0Ie	-11.84	165 ± 8	40 ± 2	253 ± 3	120 ± 6	pcyg on H α, β , central star of a compact cluster 20arcsec dia.
RP s1881	05 04 37.15	-67 49 49.0		B3IIIe	-13.86	97 ± 5	7 ± 0	284 ± 2	24 ± 1	H α , 3 stars in a row. All bright in H α
RP s1751	05 04 37.41	-69 05 05.7		B3IIIp[e]	-13.55	94 ± 5	22 ± 1	290 ± 2	40 ± 2	H α, β , [S II], [N II], [O III] possible Bp, sh
RP s1923	05 04 40.40	-66 49 49.0		B1IIIe	-13.77	187 ± 9	23 ± 1	312 ± 14	124 ± 6	H α, β
RP s1672	05 04 40.78	-70 42 06.0		B1.7Ve	-13.09	335 ± 17	56 ± 2	240 ± 5	306 ± 15	H α, β
RP s1863	05 04 44.02	-68 16 32.4		A0Ve	-13.73	181 ± 9	8 ± 0	264 ± 2	85 ± 4	H α, β , faint diffuse H II emission surrounding star
RP s1795	05 04 44.85	-68 58 31.1	L63106	B2IIIe	-12.47	205 ± 10	47 ± 2	290 ± 3	163 ± 8	H α, β
RP s1936	05 04 47.97	-66 38 53.2			-13.91	445 ± 22	134 ± 5	302 ± 13	489 ± 25	H α, β , very weak
RP s1935	05 04 51.70	-66 38 07.6		B0.5IIIe	-12.32	360 ± 18	140 ± 6	315 ± 18	401 ± 20	H α, β, γ , southern-most of 7 stars in a line
RP s1675	05 04 54.94	-70 43 33.7		B3IIIe	-12.39	330 ± 16	46 ± 2	275 ± 8	285 ± 14	H α, β
RP s1650	05 04 56.74	-70 34 45.9	L63114	B1.7Ve	-13.83	288 ± 14	35 ± 1	250 ± 4	230 ± 12	H α, β
RP s1640	05 04 58.05	-70 41 03.0	BE74519	B1.7Ve	-13.36	335 ± 17	27 ± 1	256 ± 4	259 ± 13	H α, β
RP s1901	05 04 58.48	-67 32 05.2		B2Ve	-13.35	231 ± 12	69 ± 3	360 ± 11	207 ± 10	H α, β
RP s1639	05 05 00.69	-70 41 03.4	MACHO23.3906.30	B3Ve	-13.25	379 ± 19	170 ± 7	243 ± 8	434 ± 22	H α, β
RP s1818	05 05 04.09	-68 44 40.4	2MASSJ05050415-6844407	B4Ive	-12.77	335 ± 17	101 ± 4	242 ± 5	342 ± 17	H α, β , Previously identified as delta Cepheid variable
RP s1820	05 05 22.28	-68 43 39.5		B5IIIe	-13.06	188 ± 9	101 ± 4	285 ± 3	177 ± 9	H α, β
RP s1629	05 05 25.31	-70 51 53.8		B0Ve	-13.77	298 ± 15	104 ± 4	255 ± 9	301 ± 15	H α, β
RP s1641	05 05 26.53	-70 39 45.2	MACHO23.4027.43							Not observed
RP s1642	05 05 30.41	-70 40 22.0		B1Ve	-13.72	395 ± 20	62 ± 2	246 ± 5	368 ± 18	H α, β
RP s1926	05 05 33.48	-66 51 17.9		A0Ve	-13.19	303 ± 15	156 ± 6	324 ± 16	341 ± 17	H α, β
RP s1821	05 05 39.09	-68 43 20.2	SAB561	B5IIIe	-13.16	229 ± 11	35 ± 1	243 ± 4	176 ± 9	H α, β
RP s1861	05 05 56.94	-68 20 03.2		A2IIIe	-13.04	270 ± 14	48 ± 2	307 ± 4	227 ± 11	H α, β , molecular absorption
RP s1915	05 06 08.53	-67 01 23.1		B3IIIe	-13.41	286 ± 14	48 ± 2	272 ± 3	242 ± 12	H α, β
RP s1882	05 06 26.66	-67 42 58.3		B0.5IIIe	-12.94	392 ± 20	50 ± 2	282 ± 6	355 ± 18	H α, β

RP Object	RA J2000	DEC J2000	Other Catalog Reference	Spec Type	Log F H α	FWHM H α km/s	EW H α Å	Vel. (helio) km/s	$v \sin i$ km/s	Comments
RP_s1260	05 15 10.00	-70 01 21.6		B3III[e]	-14.07	52 ± 3	61 ± 2	241 ± 1	18 ± 1	H α , β , γ , [S II], [N II], [O II]
RP_s1524	05 15 41.41	-67 58 52.4	BE74231	B4III[e]	-12.29	412 ± 21	18 ± 1	316 ± 1	302 ± 15	H α , β , γ , [S II], [N II], [O II], dense H II halo surrounding, SP
RP_s1582	05 15 45.61	-66 58 42.3		B1Ve	-14.99	42 ± 2	55 ± 2	291 ± 1	7 ± 0	H α , p cyg on H β
RP_s1469	05 15 48.74	-68 33 04.0		B1.7Ve	-13.92	98 ± 5	27 ± 1	272 ± 3	49 ± 2	H α only
RP_s1414	05 16 24.57	-68 55 27.6		B3V[e]	-12.97	302 ± 15	186 ± 7	232 ± 1	349 ± 18	H α , β , γ , [S II], [N II], [O II], Poor spectral fit
RP_s1335	05 16 27.14	-69 26 22.6	SAB1899	B1Ve	-13.41	262 ± 13	78 ± 3	219 ± 4	246 ± 12	H α , β , DP V>R
RP_s1529	05 16 31.96	-67 56 50.2		B2V[e]	-13.52	102 ± 5	21 ± 1	293 ± 2	47 ± 2	H α , β , γ , [S II], [N II], [O II]
RP_s1334	05 16 33.24	-69 31 29.2		F0Ve	-13.04	188 ± 9	102 ± 4	273 ± 3	178 ± 9	H α , β only
RP_s1423	05 16 39.06	-68 53 20.5		B3Ve	-14.57	95 ± 5	8 ± 0	238 ± 1	25 ± 1	H α only + HeI 4144 in emission
RP_s1386	05 16 39.11	-69 20 47.9	SAB899	B3Ve	-13.41	339 ± 17	79 ± 3	274 ± 4	328 ± 16	H α only, DP centre
RP_s1382	05 16 52.29	-69 33 56.4	SAB631	B1Ve	-13.37	76 ± 6	15 ± 1	291 ± 4	20 ± 5	H α , β , SP bottle-shape
RP_s1381	05 17 01.02	-69 34 10.5	SAB138	B1Ve	-12.54	226 ± 11	48 ± 2	249 ± 4	184 ± 9	H α , β , SP
RP_s1525	05 17 06.93	-68 00 27.8		B2V[e]	-13.98	134 ± 7	52 ± 2	211 ± 5	98 ± 5	H α , β , [S II], [N II]strong central H α emission, SP
RP_s1526	05 17 07.33	-68 00 18.5		B1Ve	-13.21	356 ± 18	63 ± 3	276 ± 4	328 ± 16	H α , β
RP_s1331	05 17 08.13	-69 07 02.1		B1.7V[e]	-13.10	48 ± 2	80 ± 3	267 ± 1	17 ± 1	H α , β , [N II], [S II], [O II], [O II], SP
RP_s2054	05 17 08.93	-69 32 21.1	SVHV 5717		-14.51	419 ± 21	86 ± 3	280 ± 4	424 ± 21	H α , [N II]but no [O II].
RP_s1588	05 17 31.40	-66 43 30.1		B3III[e]	-12.77	291 ± 15	149 ± 6	320 ± 1	317 ± 16	H α , β , γ , [S II], [N II], [O II]
RP_s1537	05 17 34.45	-67 50 08.8		B1IIe	-13.81	257 ± 13	42 ± 2	303 ± 4	208 ± 10	H α , β
RP_s1538	05 17 35.37	-67 46 40.3		B1Ve	-13.33	299 ± 15	78 ± 3	289 ± 4	285 ± 14	H α , β
RP_s1592	05 17 40.69	-66 42 08.8		B0III[e]	-12.82	327 ± 16	83 ± 3	196 ± 4	324 ± 16	H α , β , [S II], [N II]
RP_s1591	05 17 40.80	-66 42 04.8		B3III[e]	-12.81	216 ± 11	93 ± 4	301 ± 15	209 ± 10	H α , β , γ , [S II], [N II], [O II]
RP_s1593	05 17 40.96	-66 42 08.7		B3III[e]	-12.90	208 ± 10	157 ± 6	319 ± 1	225 ± 11	H α , β , γ , [S II], [N II]
RP_s1478	05 17 46.26	-68 30 03.2		B1Ve	-13.32	351 ± 18	49 ± 2	308 ± 5	305 ± 15	H α , β
RP_s1374	05 17 53.26	-69 11 44.1	BE74242	B2IIe	-12.66	291 ± 15	37 ± 1	292 ± 4	233 ± 12	H α , β , low [O III] 5007 from ambient emission in area
RP_s1373	05 17 57.65	-69 11 10.3	BE74242	B2IIe	-12.09	513 ± 26	106 ± 4	305 ± 10	555 ± 28	H α , β
RP_s1384	05 17 59.80	-69 30 07.6		A3IIe	-12.77	460 ± 23	60 ± 2	283 ± 13	433 ± 22	H α , β
RP_s1383	05 18 02.98	-69 29 49.1		B0Ve	-13.00	309 ± 15	32 ± 1	237 ± 3	243 ± 12	H α , β , SP
RP_s1448	05 18 08.15	-68 42 39.9		B1V[e]	-13.53	99 ± 5	51 ± 2	313 ± 2	63 ± 3	H α , β , [S II], [N II]
RP_s1503	05 18 59.76	-68 14 39.4		B1Ve	-13.47	301 ± 15	48 ± 2	261 ± 4	257 ± 13	H α , β
RP_s1514	05 19 07.79	-68 05 42.0	AL128	B1IIe	-12.63	242 ± 12	48 ± 2	303 ± 3	200 ± 10	H α , β
RP_s1517	05 19 07.91	-68 02 57.7		B1.5Ve	-14.17	319 ± 16	36 ± 1	288 ± 4	260 ± 13	H α , + [O I] 6300, 6363
RP_s1468	05 19 08.33	-68 34 01.5		B1Ve	-13.84	206 ± 10	56 ± 2	282 ± 3	170 ± 9	H α , β
RP_s1339	05 19 11.45	-69 41 55.9	SAB2069	B1Ve	-13.34	175 ± 9	45 ± 2	249 ± 3	134 ± 7	H α , β , other weak forbidden line probably from ambient emission, SP
RP_s1437	05 19 12.83	-68 44 04.6		B5.7Ve	-14.38	363 ± 18	28 ± 1	302 ± 3	284 ± 14	H α only
RP_s1506	05 19 17.99	-68 13 45.0		B1Ve	-12.94	327 ± 16	67 ± 3	309 ± 4	306 ± 15	H α , β
RP_s1479	05 19 25.11	-68 29 36.7		B3IIe	-13.55	73 ± 4	107 ± 4	271 ± 2	52 ± 3	H α , β , [S II]. H II emission extending 1 arcsec on w side of star. Companion? To immediate E.
RP_s1149	05 19 29.28	-71 15 50.7		B1.7V[e]	-12.56	245 ± 12	53 ± 2	226 ± 3	208 ± 10	H α , β weak [S II], [O III]
RP_s1436	05 19 33.68	-68 45 24.5		B1Ve	-14.10	112 ± 6	44 ± 2	274 ± 1	73 ± 4	H α only
RP_s1370	05 19 34.20	-69 57 50.6		B3Ve	-13.07	275 ± 14	33 ± 1	258 ± 3	212 ± 11	H α , β , SP
RP_s1539	05 19 37.30	-67 49 30.5	AL136	B0.5IIIe	-13.10	384 ± 19	44 ± 2	294 ± 5	338 ± 17	H α , β
RP_s1340	05 19 44.00	-69 40 28.3		B1V[e]	-13.37	56 ± 3	47 ± 2	243 ± 1	18 ± 1	H α , β , [O II], [O III], [S II], [N II], SP
RP_s1449	05 20 11.54	-68 37 53.7		F5IIe	-13.49	259 ± 13	107 ± 4	293 ± 14	264 ± 13	H α
RP_s1452	05 20 12.96	-68 38 08.3		B2Ve	-13.72	95 ± 5	26 ± 1	269 ± 1	44 ± 2	H α only
RP_s1342	05 20 15.34	-69 40 29.0		B1Ve	-14.06	117 ± 6	6 ± 0	278 ± 1	33 ± 2	H α only, SP
RP_s1600	05 20 17.83	-66 52 53.6		B2Ve	-13.14	332 ± 17	69 ± 3	313 ± 1	312 ± 16	H α , β , ([S II], [N II], [O II], [O III] from dense compact H II region 12 x 16 arcsec).
RP_s1265	05 20 34.34	-70 00 33.0		B8Ve	-13.41	214 ± 11	55 ± 2	259 ± 3	178 ± 9	H α , β
RP_s1356	05 20 39.89	-69 44 59.1	SAB2161	B1IIe	-12.71	290 ± 14	57 ± 2	259 ± 4	260 ± 13	H α , β , SP
RP_s1586	05 20 40.11	-66 48 49.2		B3Ve	-14.22	85 ± 4	13 ± 1	305 ± 1	25 ± 1	H α , β , Centre star of faint emission 25 arcsec radius.
RP_s1355	05 20 45.17	-69 58 24.5		B7Ve	-14.07	371 ± 19	36 ± 1	258 ± 3	308 ± 15	H α only, SP
RP_s1343	05 20 47.86	-69 39 56.2		A7V[e]	-13.14	272 ± 14	60 ± 2	308 ± 3	242 ± 12	H α , β , [S II], [O III], DP R>V
RP_s1238	05 20 49.08	-70 12 40.8		A3V[e]		366 ± 18	15 ± 1	305 ± 1	249 ± 12	with [O III] emission on star. No H emission. SP
RP_s1344	05 20 51.12	-69 38 28.9	BE74565	B1IIe	-12.72	486 ± 24	101 ± 4	259 ± 7	510 ± 26	H α , β , DP centre
RP_s1173	05 20 54.35	-70 49 42.1	SAB817	B1IIe	-12.66	374 ± 19	69 ± 3	225 ± 5	356 ± 18	H α , β , SP
RP_s1535	05 20 57.37	-67 49 21.1	BE74255	B3IIe	-13.29	98 ± 5	33 ± 1	304 ± 2	51 ± 3	H α , p cyg on H β , In dense H II region 20 x 14 arcsec dia
RP_s1368	05 21 05.22	-69 01 03.3		B1.5Ve	-13.46	442 ± 22	42 ± 2	281 ± 4	383 ± 19	H α only
RP_s1156	05 21 15.37	-71 05 29.8		B1Ve	-14.46	536 ± 27	24 ± 1	157 ± 3	426 ± 21	H α only
RP_s1365	05 21 16.97	-69 04 57.8		B2Ve	-13.48	324 ± 16	64 ± 3	308 ± 4	304 ± 15	H α , β

RP Object	RA J2000	DEC J2000	Other Catalog Reference	Spec Type	Log F H α	FWHM H α km/s	EW H α Å	Vel. (helio) km/s	$v \sin i$ km/s	Comments
RP605	05 27 49.37	-71 31 19.8		A1V[e]	-13.37	251 ± 13	60 ± 2	247 ± 2	221 ± 11	H $\alpha, \beta, \gamma, \delta$, [O II] 3727, [N II], [S II], [O III] 5007
RP1057	05 28 02.72	-67 31 16.5	AL 207	B2IIe	-12.18	256 ± 13	72 ± 3	324 ± 4	239 ± 12	H α, β some diffuse emission in area.
RP840	05 28 03.99	-69 09 57.2		B4IVe	-12.96	453 ± 23	70 ± 3	248 ± 17	438 ± 22	H α, β , SP
RP2185	05 28 04.23	-69 05 26.8	SVHV 2565	B0Ve	-13.89	182 ± 9	19 ± 1	294 ± 4	111 ± 6	H α, β , DP centre
RP823	05 28 04.41	-69 13 33.0		B1.7Ve	-13.17	430 ± 22	47 ± 2	241 ± 11	382 ± 19	H α, β , SP
RP822	05 28 07.61	-69 14 28.4		B1V[e]	-13.12	345 ± 17	44 ± 2	286 ± 4	300 ± 15	H α, β , [O III] 5007 weak. Possible symbiotic, SP
RP841	05 28 08.09	-69 10 22.6		B2Ve	-14.17	213 ± 12	25 ± 1	264 ± 16	146 ± 9	ambient emission brings in the [O III] 5007 line, SP, Bottle shape
RP702	05 28 14.06	-69 54 37.9		F0IIe	-12.52	394 ± 20	43 ± 2	335 ± 5	338 ± 17	H α, β , FeII 4173, 4179
RP879	05 28 20.08	-68 59 10.4		B0IIe	-12.50	155 ± 8	65 ± 3	258 ± 3	127 ± 6	H α, β , SP
RP512	05 28 20.82	-70 59 22.4	BE74589	B2IIe	-12.63	393 ± 20	32 ± 1	216 ± 22	319 ± 16	H α, β
RP2186	05 28 27.04	-69 05 37.5	BE74300	BVe	-12.73	163 ± 8	45 ± 2	294 ± 4	123 ± 6	H α, β , low [O III] due to ambient emission. SP
RP510	05 28 28.87	-71 00 48.5		B5V[e]	-13.95	84 ± 4	3 ± 0	225 ± 1	4 ± 0	H α , [N II], [S II], [O III], SP
RP796	05 28 32.24	-69 19 56.8		B1Ve	-13.83	278 ± 14	32 ± 1	280 ± 3	215 ± 11	H α, β, γ
RP472	05 28 36.50	-70 56 21.4		B2IIe	-11.92	341 ± 17	49 ± 2	225 ± 5	296 ± 15	H α, β, γ , H ϵ l absorption
RP436	05 28 36.57	-70 48 25.9		B2IIe	-13.14	401 ± 20	39 ± 2	187 ± 6	344 ± 17	H α, β only
RP839	05 28 38.27	-69 11 07.6	BE74307	B0IIe	-12.31	239 ± 12	35 ± 1	264 ± 4	185 ± 9	H α, β, γ , SP
RP688	05 28 40.90	-70 01 38.1	MACHO77.7788.54	B2IIe	-12.99	329 ± 16	59 ± 2	203 ± 5	300 ± 15	H α, β
RP2179	05 28 45.59	-68 59 23.7		BIVe	-12.78	157 ± 8	63 ± 3	285 ± 5	130 ± 7	H α, β , close to H II region. DP centre
RP2181	05 28 48.85	-69 01 19.6		BIII[e]	-12.69	297 ± 15	56 ± 2	283 ± 5	260 ± 13	H α, β , [O III], in H II region, SP
RP784	05 28 53.10	-69 24 51.4	MACHO77.7918.68	B3Ve	-13.87	129 ± 6	25 ± 1	272 ± 3	73 ± 4	H α, β
RP783	05 28 57.69	-69 25 09.5	MACHO77.7918.92	A7III[e]	-13.84	288 ± 14	31 ± 1	258 ± 5	224 ± 11	H α, β , [O III]
RP2182	05 28 58.82	-69 03 55.0		BVe	-13.84	377 ± 19	57 ± 2	276 ± 4	349 ± 18	H α, β , in H II region. SP
RP794	05 29 01.97	-69 22 50.6	BE74309	B1IIe	-12.20	184 ± 9	100 ± 4	274 ± 3	174 ± 9	H α, β, γ , Bpe
RP2183	05 29 02.92	-69 04 29.1		BIIIe	-14.11	242 ± 12	43 ± 2	281 ± 3	193 ± 10	H α, β , in H II region, SP
RP880	05 29 07.24	-69 04 51.3		B1.5V[e]	-13.73	175 ± 9	88 ± 4	278 ± 2	158 ± 8	H α, β , most [S II], [N II], [O II], [O III] from ambient H II emission in area. DP R>V
RP838	05 29 21.10	-69 11 17.8		B1Ve	-13.96	163 ± 8	16 ± 1	269 ± 2	92 ± 5	H α only but mainly from ambient emission, SP
RP887	05 29 22.39	-69 00 11.8		B3Ve	-13.88	347 ± 17	29 ± 1	272 ± 2	270 ± 14	H $\alpha, \beta, \gamma, [O III], [N II], [S II]$, DP V>R
RP836	05 29 22.71	-69 10 13.8	BE74313	B0.5IIe	-12.47	207 ± 10	27 ± 1	272 ± 3	146 ± 7	H α, β , weak [O III], SP
RP995	05 29 28.71	-68 28 29.9		B3V[e]	-13.96	97 ± 5	52 ± 2	273 ± 1	61 ± 3	H α, β ambient emission producing [S II], [N II], [O II] and [O III]
RP1056	05 29 41.19	-67 35 48.2	AL 233	B3IIe	-13.09	297 ± 15	32 ± 1	291 ± 5	232 ± 12	H α, β
RP864	05 29 41.40	-69 06 53.4		B5IIe	-12.83	312 ± 16	27 ± 1	217 ± 10	239 ± 12	H α, β only
RP835	05 29 50.72	-69 10 32.0		B1Ve	-13.62	85 ± 11	12 ± 3	258 ± 3	23 ± 10	H α, β , [O III] from ambient emission, SP, Bottle shape
RP2177	05 29 51.32	-68 59 15.5		BIIIe	-12.69	350 ± 18	48 ± 2	288 ± 4	305 ± 15	H α, β , SP
RP785	05 29 55.03	-69 26 53.3		B0V[e]	-13.25	227 ± 11	57 ± 2	257 ± 3	196 ± 10	H α, β , [O III], SP
RP2210	05 29 56.15	-68 38 50.1		B1V[e]	-12.73	250 ± 13	26 ± 1	318 ± 10	184 ± 9	H $\alpha, \beta, \gamma, [O III], [N II], [S II]$
RP974	05 30 00.60	-67 57 30.1		B3Ve	-13.94	202 ± 10	72 ± 3	284 ± 3	181 ± 9	H α, β
RP786	05 30 01.22	-69 28 09.5	SAB955	B3IIe	-13.01	224 ± 11	27 ± 1	266 ± 3	161 ± 8	H α, β
RP740	05 30 01.79	-69 40 46.6	SAB1210	B3V[e]	-13.27	179 ± 9	56 ± 2	275 ± 2	147 ± 7	H α, β , [S II], [N II], [O III], SP
RP1083	05 30 14.61	-66 49 12.7	AL243	B2IIe	-12.42	395 ± 20	88 ± 4	355 ± 6	398 ± 20	H α, β
RP546	05 30 19.08	-71 20 04.6		B5Ve	-12.49	453 ± 23	56 ± 2	244 ± 3	426 ± 21	H α, β
RP1077	05 30 24.32	-67 14 54.6	BE74, 75	B2IIe	-12.93	350 ± 17	70 ± 3	323 ± 5	330 ± 17	H α, β
RP667	05 30 26.08	-70 15 07.2		A4IVe	-13.77	59 ± 3	25 ± 1	275 ± 2	13 ± 1	Possible AGB star. Variable.
RP867	05 30 26.65	-69 05 35.8		B3Ve	-13.31	312 ± 16	46 ± 2	265 ± 1	268 ± 13	H α, β
RP1079	05 30 33.33	-66 57 41.9		A0V[e]	-14.07	246 ± 12	54 ± 2	287 ± 2	210 ± 11	H α + [O III]
RP788	05 30 39.18	-69 25 43.8		F8IIe	-13.89	119 ± 6	9 ± 0	270 ± 1	44 ± 2	H α, β , ambient emission causing [S II] & [O III], Cepheid known, SP
RP930	05 30 39.36	-68 34 03.6		B1.7Ve	-13.17	335 ± 17	33 ± 1	280 ± 2	266 ± 13	H α , other forbidden lines: [N II], [S II], [O III] but thick nebula in immediate area.
RP2203	05 30 39.43	-68 35 28.5					0			Not observed
RP787	05 30 40.67	-69 25 31.1	MACHO77.8160.6	B3IIe	-12.69	422 ± 21	38 ± 2	276 ± 6	355 ± 18	H α, β
RP834	05 30 41.64	-69 11 34.6		B1.5IIe	-13.10	99 ± 5	15 ± 1	256 ± 1	38 ± 2	H α, β , DP centre
RP587	05 30 43.25	-70 25 57.9		B3Ve	-13.11	294 ± 15	42 ± 2	256 ± 4	243 ± 12	H α, β
RP556	05 30 55.02	-70 45 28.2	MACHO7.8140.15	B2IIe	-12.18	214 ± 11	55 ± 2	255 ± 3	178 ± 9	H α, β , SP
RP1075	05 31 04.25	-67 08 22.3		B2IIe	-12.89	362 ± 18	77 ± 3	315 ± 5	352 ± 18	H α, β
RP881	05 31 10.07	-69 05 25.0		B1V[e]	-13.62	68 ± 3	28 ± 1	263 ± 25	22 ± 1	H α, β, γ , [O III], [N II], [S II]. Within ambient H II which contributes to nebula lines, SP
RP824	05 31 10.86	-69 14 16.9		B8V[e]	-13.77	199 ± 10	21 ± 1	270 ± 3	129 ± 7	H α, β , [S II], [O III]
RP444	05 31 15.62	-70 53 48.4	XMMUJ053115.4-705350	B0Ie	-13.13	345 ± 17	14 ± 1	269 ± 4	232 ± 12	H α, β , high mass X-ray binary
RP2209	05 31 16.89	-68 40 05.9		B3III[e]	-13.07	194 ± 10	11 ± 0	295 ± 8	102 ± 5	H $\alpha, \beta, [O III], [N II], [S II]$
RP443	05 31 18.75	-70 54 07.7	BE74595	B3IVe	-12.51	415 ± 21	84 ± 3	268 ± 4	420 ± 21	H α, β

RP Object	RA J2000	DEC J2000	Other Catalog Reference	Spec Type	Log F H α	FWHM H α km/s	EW H α Å	Vel. (helio) km/s	$v \sin i$ km/s	Comments
RP364	05 35 49.19	-66 51 26.0		B1.5Ve	-13.86	329 ± 16	28 ± 1	302 ± 5	254 ± 13	H α
RP365	05 35 53.94	-66 52 32.3		F8Ve	-13.58	399 ± 20	65 ± 3	262 ± 6	382 ± 19	H α, β , some local faint H II emission
RP368	05 35 55.73	-66 51 08.6		B2IVe	-13.33	271 ± 14	28 ± 1	335 ± 4	203 ± 10	H α, β
RP369	05 35 57.84	-66 50 53.7	AL350	B7IIIe	-13.56	281 ± 14	30 ± 1	282 ± 4	217 ± 11	H α, β
RP1033	05 36 04.27	-67 55 37.0	BE74385	B2IVe	-11.05	263 ± 13	54 ± 2	289 ± 4	227 ± 11	H α, β , LBV poss
RP487	05 36 04.46	-70 51 01.4	BE74605	B2IIe	-12.89	394 ± 20	49 ± 2	223 ± 16	347 ± 17	H α, β, γ
RP684	05 36 09.68	-70 06 08.0	SAB1386	B7Ve	-13.59	464 ± 23	34 ± 1	224 ± 5	394 ± 20	H α only
RP1005	05 36 16.32	-70 26 21.9	MACHO11.9112.61	B3V[e]	-13.18	223 ± 11	110 ± 4	322 ± 3	223 ± 11	H α, β , [O III], SP
RP531	05 36 16.96	-71 09 41.9		B2Ve	-13.98	524 ± 26	41 ± 2	329 ± 2	461 ± 23	H α, β
RP348	05 36 28.63	-66 53 02.5	AL359	B5IIIe	-12.46	509 ± 25	67 ± 3	312 ± 9	497 ± 25	H α, β
RP370	05 36 33.18	-66 51 18.6		B1Ve	-13.65	379 ± 19	45 ± 2	286 ± 5	332 ± 17	H α, β
RP639	05 36 37.12	-69 22 09.4		B3IIIe	-12.87	135 ± 7	40 ± 2	245 ± 3	92 ± 5	H α, β [O III] is ambient emission
RP557	05 36 39.75	-70 44 37.4		B3Ve	-14.18	433 ± 22	45 ± 2	238 ± 4	385 ± 19	H α, β
RP258	05 36 43.71	-69 36 44.6	MACHO81.9125.21	B3III[e]	-12.87	180 ± 9	32 ± 1	274 ± 3	126 ± 6	H α, β, γ , [O III], [O II], [N II], [S II]. Within H II region, SP
RP259	05 36 48.63	-69 26 44.6		B3V[e]	-13.54	218 ± 11	62 ± 2	333 ± 18	187 ± 9	H α, β, γ , [O III], [O II], [N II], [S II]
RP231	05 36 49.38	-69 23 55.2		B2V[e]	-13.09	246 ± 12	53 ± 2	265 ± 22	210 ± 11	H α, β, γ , [O III], [O II], [N II], [S II]
RP2163	05 36 54.13	-66 30 04.1		B3Ve	-13.59	176 ± 9	62 ± 2	320 ± 7	145 ± 7	H α, β
RP330	05 36 57.68	-67 34 02.6		B1Ve	-13.83	166 ± 8	15 ± 1	291 ± 2	91 ± 5	H α , (pc on H β), faint, ambient H II
RP284	05 37 12.85	-68 37 11.8		B1Ve	-12.89	465 ± 23	74 ± 3	265 ± 15	463 ± 23	H α, β
RP353	05 37 14.27	-66 26 59.2		B3IV[e]	-13.08	212 ± 11	91 ± 4	263 ± 5	199 ± 10	H α, β, γ , [O III], [O II], [N II], [S II]
RP352	05 37 14.60	-66 26 52.6		B1V[e]	-12.80	38 ± 2	129 ± 5	291 ± 1	13 ± 1	strong [S II] + [N II] but low [O III]. Strong [O II]
RP27	05 37 25.41	-70 30 47.9		A4Ve	-13.58	166 ± 8	136 ± 5	254 ± 3	168 ± 8	H α, β , DP V>R
RP298	05 37 28.44	-68 12 34.7		A2IVe	-13.09	518 ± 26	101 ± 4	278 ± 8	546 ± 27	H α, β
RP257	05 37 35.37	-69 34 59.5	LI-SMC302	B2IIe	-12.11	282 ± 14	172 ± 7	268 ± 5	315 ± 16	H α, β , Low level [S II], [O III] probably ambient
RP29	05 37 38.98	-70 32 46.3		B1.7Ve	-13.50	555 ± 28	31 ± 1	271 ± 65	466 ± 23	H α, β
RP1043	05 37 40.59	-67 31 37.1		B1Ve	-14.01	111 ± 6	8 ± 0	293 ± 1	36 ± 2	H α only. Centre of faint elliptical emission 20.7 x 42 arcsec
RP283	05 37 48.30	-68 39 54.6		B3V[e]	-13.16	496 ± 25	41 ± 2	292 ± 19	435 ± 22	H α, β, γ , [O III], [N II], [S II], DP V>R
RP372	05 37 50.31	-66 55 40.2		B4IIIe	-12.98	394 ± 20	41 ± 2	306 ± 5	338 ± 17	H α, β
RP285	05 37 58.73	-68 33 39.2	BE74411	B2IVe	-12.50	352 ± 18	38 ± 2	261 ± 4	290 ± 15	H α, β
RP226	05 38 03.07	-69 31 58.9		B1.7V[e]	-12.85	49 ± 2	25 ± 1	267 ± 2	4 ± 0	H α, β , forbidden lines from ambient emission
RP81	05 38 03.78	-70 50 28.3		B0IVe	-12.70	307 ± 15	27 ± 1	251 ± 18	234 ± 12	H α, β
RP634	05 38 04.67	-69 59 18.4		B6Ve	-13.54	226 ± 11	96 ± 4	242 ± 3	220 ± 11	H α, β , SP
RP2198	05 38 07.83	-70 01 37.8								Not observed
RP338	05 38 12.92	-67 18 27.8		B2Ve	-13.81	205 ± 10	42 ± 2	303 ± 2	159 ± 8	H α, β , low levels (2 σ noise) due to faint ambient emission.
RP337	05 38 15.55	-67 15 49.2		B3IIIe	-13.03	276 ± 14	60 ± 2	267 ± 4	246 ± 12	H α, β
RP224	05 38 17.32	-69 32 05.0		B0.5I[e]	-12.41	141 ± 7	41 ± 2	260 ± 3	98 ± 5	H α, β , [S II], [N II], [O III], [O II]
RP335	05 38 17.82	-67 34 39.8		B2IIe	-13.03	240 ± 12	46 ± 2	256 ± 3	198 ± 10	H α, β
RP301	05 38 19.82	-67 45 01.5		B1V[e]	-13.36	135 ± 7	76 ± 3	314 ± 2	111 ± 6	H α, β , [S II], [N II], [O II]
RP1952	05 38 22.79	-71 15 13.5		B9Ve	-14.25	511 ± 26	42 ± 2	201 ± 1	449 ± 23	H α only
RP91	05 38 22.87	-70 18 01.5		B1Ve	-14.32	335 ± 17	26 ± 1	233 ± 2	252 ± 13	H α only
RP146	05 38 26.35	-70 10 50.0		B2Ve	-14.02	534 ± 27	51 ± 2	223 ± 2	496 ± 25	H α only
RP290	05 38 40.83	-68 24 00.7		BVp[e]	-11.92	148 ± 7	124 ± 5	267 ± 3	143 ± 7	H α, β , [O III]
RP311	05 38 44.16	-68 43 53.9		B1IVe	-12.58	264 ± 13	53 ± 2	317 ± 4	227 ± 11	H α, β , forbidden lines due top strong ambient emission
RP325	05 38 49.92	-67 32 04.5		B2Ve	-13.73	285 ± 14	29 ± 1	317 ± 4	215 ± 11	H α, β
RP256	05 38 51.35	-69 44 51.1		B0.5Ve	-13.47	48 ± 2	24 ± 1	267 ± 1	4 ± 0	H α, β , [S II], [O III], large halo probably associated.
RP248	05 38 51.39	-69 21 42.5		B2V[e]	-13.10	151 ± 8	56 ± 2	264 ± 2	119 ± 6	H α, β, γ , [S II], [N II], [O II], [O III] at least, SP 50% forbidden lines from ambient emission
RP339	05 38 55.12	-67 19 31.7		B1Ve	-12.38	346 ± 17	57 ± 2	340 ± 4	317 ± 16	H α, β
RP104	05 39 03.10	-70 23 43.9		B1V[e]	-12.80	198 ± 10	38 ± 2	241 ± 3	147 ± 7	H α , [N II] and [S II]
RP1034	05 39 12.67	-67 42 49.9		B3Ve	-12.72	310 ± 16	50 ± 2	286 ± 4	273 ± 14	H α
RP66	05 39 14.02	-70 45 03.7		B1Ve	-13.66	226 ± 11	31 ± 1	245 ± 2	168 ± 8	H α, β
RP340	05 39 16.59	-67 23 42.9	BE74141	B5IIIe	-12.42	289 ± 14	59 ± 2	304 ± 4	260 ± 13	H α, β
RP391	05 39 19.80	-67 08 55.7		B3Ve	-12.83	249 ± 12	70 ± 3	325 ± 2	225 ± 11	H α, β
RP286	05 39 25.87	-68 33 16.2	BE74426	B1Ve	-13.48	458 ± 23	31 ± 1	253 ± 3	378 ± 19	H α, β, γ
RP390	05 39 36.81	-67 08 33.6		B3IIIe	-13.92	244 ± 12	35 ± 1	295 ± 2	190 ± 10	H α , [S II]
RP92	05 39 37.63	-70 15 43.9	SAB507	B0IIIe	-13.12	357 ± 18	104 ± 4	269 ± 6	366 ± 18	H α, β
RP141	05 39 40.03	-70 10 16.7		B1Ve	-14.19	143 ± 11	30 ± 1	240 ± 2	93 ± 5	H α , Bottle shape
RP632	05 39 44.61	-70 01 00.9		B1Ve	-13.87	102 ± 24	11 ± 2	262 ± 5	36 ± 21	H α, β , SP, Bottle shape
RP341	05 39 48.49	-67 23 23.5		B2Ve	-13.28	184 ± 9	41 ± 2	295 ± 3	139 ± 7	H α, β

RP Object	RA J2000	DEC J2000	Other Catalog Reference	Spec Type	Log F H α	FWHM H α km/s	EW H α Å	Vel. (helio) km/s	$v \sin i$ km/s	Comments
RP83	05 40 04.53	-70 39 44.9	SAB1449	B0IIe	-13.38	108 ± 5	16 ± 1	255 ± 2	48 ± 2	H α, β , Forbidden lines due to surrounding thick H II disk 16arcsec radius
RP8138	05 40 10.00	-70 09 20.1		B3Ve	-13.50	62 ± 3	22 ± 1	270 ± 1	14 ± 1	H α only
RP8139	05 40 12.00	-70 09 15.1		F0III[e]	-13.84	411 ± 21	43 ± 2	314 ± 5	354 ± 18	H α , [S II], SP
RP8625	05 40 15.33	-70 46 13.2		B1Ve	-13.51	543 ± 27	44 ± 2	221 ± 9	493 ± 25	H α, β
RP8288	05 40 19.60	-68 29 19.9			-13.42	515 ± 26	37 ± 1		441 ± 22	H α, β
RP821	05 40 19.65	-70 13 47.3		A6IVe	-14.98	50 ± 2	114 ± 5	220 ± 2	25 ± 1	Low emission levels at time of observation
RP8160	05 40 24.80	-69 57 15.5		B8Ie	-12.51	311 ± 16	37 ± 1	268 ± 2	252 ± 13	H α , ([S II] from large H II disk R=18 arcsec)
RP8387	05 40 25.58	-67 07 55.6		B3Ve	-13.35	271 ± 14	40 ± 2	310 ± 4	221 ± 11	H α, β
RP82197	05 40 26.74	-70 07 18.5			-14.25	177 ± 9	8 ± 0		82 ± 4	H α , DP R>V
RP81029	05 40 26.95	-68 09 40.3		A3Ve	-13.68	281 ± 14	73 ± 3	261 ± 4	266 ± 13	H α, β
RP8629	05 40 37.20	-70 09 09.8		B1V[e]	-13.26	74 ± 4	26 ± 1	241 ± 2	26 ± 1	H $\alpha, H\beta$ absorbed, bright emission extending 6 arcsec around star with [S II], [N II][O II]
RP8239	05 40 39.38	-69 15 29.8	BE74441	B0.5IIIe	-12.57	264 ± 13	68 ± 3	260 ± 4	241 ± 12	Pcyg on H α, β
RP81032	05 40 49.76	-67 57 22.5		B1.7V[e]	-13.93	195 ± 10	40 ± 2	301 ± 2	149 ± 8	H α, β , [S II], [O II]
RP8236	05 40 50.29	-69 21 26.3	BE74443	B0V[e]	-13.14	118 ± 6	49 ± 2	254 ± 2	79 ± 4	H α, β , [S II], [N II], [O II], [O III]
RP8115	05 40 50.99	-70 36 37.9		B3IIIe	-14.20	281 ± 14	5 ± 0	247 ± 1	136 ± 7	H α , low level [S II]
RP8306	05 40 51.97	-68 55 09.9		B0.5III[e]	-12.58	122 ± 6	37 ± 1	252 ± 2	76 ± 4	H α, β, γ , [S II], [N II], [O II], [O III] in H II
RP8240	05 40 55.46	-69 14 09.9		B0.5V[e]	-13.06	159 ± 8	40 ± 2	259 ± 17	115 ± 6	H α, β , [S II], [N II], [O II], [O III]
RP8238	05 40 55.93	-69 16 14.5	BE74444	B0.5III[e]	-12.10	293 ± 15	116 ± 5	246 ± 28	304 ± 15	H α, β , [S II]
RP8237	05 41 00.76	-69 22 05.1	BE74443	B1V[e]	-13.01	152 ± 8	35 ± 1	251 ± 3	104 ± 5	H α, β , [S II], [N II], [O II], [O III]
RP896	05 41 04.59	-70 19 58.4	SAB973	B8V[e]	-13.87	374 ± 19	35 ± 1	252 ± 1	310 ± 16	H α, β , [S II], [N II]
RP8113	05 41 05.19	-70 32 31.0		B1Ie	-13.77	206 ± 10	29 ± 1	228 ± 1	145 ± 7	H α only
RP856	05 41 10.12	-70 53 38.7		B1Ie	-13.24	135 ± 7	5 ± 0	244 ± 99	45 ± 2	H α only
RP895	05 41 13.73	-70 23 24.7		B9V[e]	-13.96	84 ± 4	72 ± 3	254 ± 16	56 ± 3	H α, β , [S II], [N II], [O II], [O III](diffuse emission at location)
RP8159	05 41 15.29	-69 58 10.3		B3IIIe	-13.32	347 ± 17	23 ± 1	255 ± 2	255 ± 13	H $\alpha, [S II]$ centre of large H II disk 22 arcsec radius
RP8343	05 41 20.97	-67 22 02.9		B1.5Ve	-14.01	358 ± 18	56 ± 2	315 ± 4	321 ± 16	H α, β
RP81022	05 41 22.94	-68 36 24.9		F0IIIe	-12.71	482 ± 24	95 ± 4	292 ± 12	506 ± 25	H α, β
RP81036	05 41 30.41	-68 53 44.0		B2IIIe	-12.21	342 ± 17	60 ± 2	268 ± 4	313 ± 16	H α, β
RP820	05 41 31.63	-70 15 31.4		B1.7Ve	-13.15	241 ± 12	40 ± 2	249 ± 3	192 ± 10	H α on star
RP8260	05 41 34.57	-68 56 02.7		F8V[e]	-14.96	148 ± 7	59 ± 2	257 ± 2	116 ± 6	H α, β , [S II], [N II], [O II], [O III]
RP8355	05 41 36.91	-66 41 57.3		B5IIIe	-13.05	190 ± 9	28 ± 1	276 ± 3	130 ± 7	H α, β with Pcyg profile.
RP863	05 41 40.07	-70 43 55.4		B2Ve	-13.47	541 ± 27	56 ± 2	262 ± 6	516 ± 26	H α, β , continuum very weak
RP81963	05 41 42.41	-71 21 18.5		B0IVe	-11.44	75 ± 4	119 ± 5	241 ± 2	57 ± 3	H $\alpha, \beta, \gamma, \delta, \epsilon$ connected to H II region to north
RP81027	05 41 43.34	-68 14 48.7		B1Ve	-13.55	284 ± 14	70 ± 3	259 ± 4	262 ± 13	H α, β
RP8300	05 41 45.26	-67 43 41.2	AL395	B0IVe	-12.95	370 ± 19	67 ± 3	293 ± 5	352 ± 18	H α, β
RP8282	05 41 45.42	-68 42 30.4		B3IIIe	-12.76	221 ± 11	51 ± 2	266 ± 3	184 ± 9	H α, β
RP81023	05 41 45.82	-68 34 32.0	BE74451	A5Ve	-13.94	537 ± 27	31 ± 1	260 ± 3	450 ± 23	H α, β
RP8377	05 41 49.44	-66 58 20.1		A3Ve	-14.07	194 ± 10	43 ± 2	261 ± 15	148 ± 7	H α
RP8276	05 41 57.35	-68 47 46.8		B1.7Ve	-13.35	341 ± 17	57 ± 2	290 ± 4	313 ± 16	H α, β
RP8354	05 41 58.11	-67 30 39.0		B1Ve	-13.09	379 ± 19	56 ± 2	247 ± 1	351 ± 18	H α , H β , H γ
RP8124	05 42 03.05	-70 44 21.9	SAB678	B0.5IIIe	-13.19	174 ± 9	40 ± 2	254 ± 3	129 ± 7	H α, β, γ
RP8280	05 42 08.95	-68 41 50.8		B2IIIe	-12.50	326 ± 16	63 ± 3	293 ± 5	298 ± 15	H α, β
RP8386	05 42 15.04	-67 07 25.9		B1Ve	-11.75	322 ± 16	56 ± 2	307 ± 3	293 ± 15	H α, β Pcyg profile on both.
RP81020	05 42 18.08	-68 37 51.4		B1Ve	-13.15	550 ± 28	60 ± 2	286 ± 8	526 ± 26	H α, β, γ
RP81112	05 42 19.59	-67 18 58.0		B1Ve	-13.47	536 ± 27	86 ± 3	310 ± 2	552 ± 28	H α, β
RP8385	05 42 25.60	-67 08 42.0		B1Ve	-13.68	279 ± 14	37 ± 1	299 ± 3	223 ± 11	H α only
RP8293	05 42 27.21	-68 17 46.0		B1Ve	-12.76	356 ± 18	144 ± 6	334 ± 5	396 ± 20	H α, β
RP81949	05 42 28.75	-68 16 48.2		B0Ve	-13.85	242 ± 12	78 ± 3	256 ± 4	225 ± 11	H α . At outer rim of globular cluster
RP811	05 42 47.38	-70 28 48.9		B0IIIe	-12.49	364 ± 18	65 ± 3	251 ± 4	345 ± 17	H α, β
RP81026	05 42 47.40	-68 32 57.4		F0Ve	-14.05	415 ± 21	50 ± 2	299 ± 7	378 ± 19	H α
RP8249	05 42 57.60	-69 16 32.9		B1.7V[e]	-12.19	100 ± 5	99 ± 4	270 ± 1	80 ± 4	H α, β, γ [S II], [N II], [O II], [O III]. Very strong emission lines
RP8307	05 43 12.41	-67 50 53.4		B1.5V[e]	-13.25	189 ± 9	28 ± 1	305 ± 19	130 ± 7	H α, β , [S II], [N II], [O II], [O III]
RP8161	05 43 14.37	-69 59 10.4		B1.7V[e]	-13.21	320 ± 16	43 ± 2	278 ± 1	268 ± 13	H α, β , [S II], [N II], [O II]
RP8309	05 43 20.77	-67 49 44.6		B1.7V[e]	-12.99	181 ± 9	35 ± 1	304 ± 2	131 ± 7	H α, β , [S II], [N II], [O II], [O III]
RP8204	05 43 51.09	-69 05 54.9	SHV0544120 -690705	B2V[e]	-13.25	137 ± 7	11 ± 0	280 ± 2	62 ± 3	H α, β , [S II], [N II], [O II], [O III]
RP8287	05 44 12.00	-68 27 27.1	BE74468	B0Ve	-12.87	330 ± 16	66 ± 3	270 ± 4	310 ± 16	H α, β
RP8322	05 44 14.25	-67 29 59.9		B2IVe	-13.18	305 ± 15	69 ± 3	307 ± 4	283 ± 14	H α, β
RP8321	05 44 20.90	-67 25 33.8		B3IVe	-12.58			295 ± 1		H α, β , pcyg on H β , extended diffuse emission

RP Object	RA J2000	DEC J2000	Other Catalog Reference	Spec Type	Log F H α	FWHM H α km/s	EW H α Å	Vel. (helio) km/s	$v \sin i$ km/s	Comments	
RP _s 274	05 44 41.56	-68 51 29.3		B1Ve	-12.63	527 ± 26	61 ± 2	259 ± 6	502 ± 25	H α, β	
RP _s 344	05 44 47.54	-67 19 33.8	IRAS - P.C05448-6720	B1.5V[e]	-13.27	95 ± 5	160 ± 6	294 ± 2	87 ± 4	H α, β , [S II], [N II], [O II]	
RP _s 131	05 44 49.65	-70 08 26.1				-13.49	212 ± 11	19 ± 1	262 ± 11	136 ± 7	weak continuum, H α, β , [O III]
RP _s 383	05 45 08.11	-67 05 58.1		B2Ve	-13.25	293 ± 15	45 ± 2	306 ± 4	250 ± 13	H α, β	
RP _s 244	05 45 19.02	-69 48 02.4		B3Ve	-13.65	330 ± 16	43 ± 2	243 ± 24	277 ± 14	H α, β , ([S II] ambient)	
RP _s 174	05 45 24.39	-69 50 09.8	BE74474	B3V[e]	-13.90	107 ± 5	90 ± 4	254 ± 4	84 ± 4	H α, β , [S II], [N II], [O II], Very low [O III]	
RP _s 255	05 45 29.40	-69 22 37.3			B0.5IIIe	-12.28	136 ± 7	46 ± 2	249 ± 3	97 ± 5	H α, β, γ
RP _s 294	05 45 29.63	-68 11 45.8			B0.5IIIe	-11.88	308 ± 15	143 ± 6	340 ± 4	339 ± 17	H α, β, γ
RP _s 262	05 45 44.23	-69 14 05.1			B2IVe	-12.55	230 ± 11	122 ± 5	274 ± 3	238 ± 12	H α, β , own emission but within H II region
RP _s 636	05 45 48.11	-69 38 32.6			B5III[e]	-13.66	349 ± 17	50 ± 2	263 ± 4	312 ± 16	H α, β , [N II], [O II], [O III], Very low [S II]
RP _s 261	05 45 58.15	-69 08 57.5			B0.5III[e]	-12.50	112 ± 6	30 ± 1	231 ± 19	62 ± 3	H α, β, γ , [S II], [N II], [O II], [O III] dense emission halo + some diffuse in area
RP _s 305	05 46 01.62	-67 35 54.9			B5IIIe	-12.54	270 ± 13	56 ± 2	265 ± 157	233 ± 12	H α
RP _s 1948	05 46 04.82	-68 27 41.1		B3IIIe	-13.63	460 ± 23	31 ± 1	342 ± 4	380 ± 19	H α , central star of faint diffuse emission 20 arcsec radius	
RP _s 1017	05 46 27.15	-68 43 15.9		B1Ve	-12.82	388 ± 19	49 ± 2	282 ± 2	350 ± 18	H α, β	
RP _s 1041	05 47 19.53	-70 04 31.4		B3Ve	-14.08	296 ± 15	17 ± 1	244 ± 1	199 ± 10	H α , [S II] from faint, extended emission	
RP _s 1947	05 47 29.74	-68 39 46.0		B3IIIe	-12.75	229 ± 11	38 ± 2	273 ± 3	176 ± 9	H α, β	
RP _s 1950	05 48 32.75	-68 13 10.8		B0Ve	-13.67	439 ± 22	116 ± 5	306 ± 5	471 ± 24	H α, β	
RP _s 211	05 48 40.08	-69 12 00.8		B5IIIe	-12.64	301 ± 15	42 ± 2	255 ± 5	250 ± 13	H α, β	
RP _s 1035	05 48 43.48	-67 36 10.6		B8III[e]	-10.03	229 ± 11	47 ± 2	284 ± 3	187 ± 9	H $\alpha, \beta, \gamma, \delta, \epsilon$, [S II], [N II], [O III], LBV poss, SP	
RP _s 210	05 49 10.14	-69 11 03.9		B2Ve	-12.87	265 ± 13	37 ± 1	248 ± 4	209 ± 10	H α, β	
RP _s 633	05 49 41.16	-70 01 36.3		B5IIIe	-13.38	98 ± 5	22 ± 1	209 ± 1	44 ± 2	H α, β , [O III] from triangular-shaped H II region to N and west	
RP _s 17	05 50 08.52	-70 09 49.4		B1.7Ve	-13.21	200 ± 10	58 ± 2	219 ± 3	168 ± 8	H α, β , some low [O III] from diffuse local H II	

notes: AL: Andrews A.D., Lindsay E.M., (1964); AGPRS: Melchior A.-L., Hughes S.M.G., Guibert J., (2000); BE74: Bohannan B., Epps H. W., (1974); FAUST: Bowyer S., Sasseen T.P., Wu X., Lampton M., (1995); GRV: Reid N., Glass I.S., Catchpole R.M., (1988); HD: Draper H., (1924); IRAS: <http://irsa.ipac.caltech.edu/IRASdocs/iras.html>; KDM: Kontizas E., Dapergolas A., Morgan D. H., Kontizas M., (2001); L63: Lindsay E.M., (1963); LI: Schwering P.B.W., (1989); MACHO: Keller S.C., Bessell M.S., Cook K. H., Geha M., Syphers D., (2002); S: Henize K.G., (1956); SAB: Sabogal B.E., Mennickent R.E., Pietrzynski G., Gieren W., (2005); SV (DV, HV): Butler C.J., Wayman P.A., (1974); SHV: Hughes S.M.G., (1989); XMMU: Lumb D.H., Guainazzi M., Gondoin P., (2001); 2MASS: Skrutskie M.F. et al. (2006)

This paper has been typeset from a $\text{T}_\text{E}\text{X}$ / $\text{L}^\text{A}\text{T}_\text{E}\text{X}$ file prepared by the author.